FT

Physikalisch Technische Bundesanstalt

Wayne D. Newhauser. Ulrich J. Schrewe and Burkhard Wiegel

Gas-to-wall Absorbed Dose Conversion Factors for Neutron Energies of 25 to 250 MeV

Die Serien der PTB-Berichte:

Atomphysik	PTB-APh
Dosimetrie	PTB-Dos
Elektrizität	PTB-E
Elektronische Entwicklung	PTB-EW
Fertigungsmeßtechnik	PTB-F
Informationstechnik	PTB-IT
Literaturzusammenstellungen und Veröffentlichungshinweise	PTB-L
Mechanik und Akustik	PTB-MA
Medizinische Meßtechnik	PTB-MM
Neutronenphysik	PTB-N
Internationale Organisation für Gesetzliches Meßwesen	PTB-OIML
Optik	PTB-Opt
Physikalische Grundlagen	PTB-PG
Radioaktivität	PTB-Ra
Technisch-Wissenschaftliche Dienste	PTB-TWD
Thermodynamik	PTB-W

Ausgelaufene Serien:

Akustik	(bis 1985)	PTB-Ak
Forschungs- und Meßreaktor Braunschweig	(bis 1988)	PTB-FMRB
Institut Berlin	(bis 1985)	PTB-IB
Mechanik	(bis 1985)	PTB-Me
Neutronendosimetrie	(bis 1988)	PTB-ND
Sicherstellung und Endlagerung radioaktiver Abfälle	(bis 1989)	PTB-SE

Physikalisch-Technische Bundesanstalt

Neutronenphysik

PTB-Bericht N-25

**Gas-to-wall Absorbed Dose Conversion Factors for
Neutron Energies of 25 to 250 MeV**

by

Wayne D. Newhauser, Ulrich J. Schrewe and Burkhard Wiegel

Abstract

Cavity chamber absorbed dose measurements do not usually strictly adhere to the conditions of the Fano theorem and therefore corrections must be made to account for differences in the gas and wall mass stopping powers. Values of gas-to-wall absorbed dose conversion factors $r_{m,g}$ were calculated for neutron energies of 25 to 250 MeV for detectors with walls of C, O, Mg, Al, Si, Fe, Zr, AlN, Al_2O_3, SiO_2, ZrO_2 and A-150 tissue-equivalent (TE) plastic and with cavity of acetylene, air, Ar, an $Ar-CO_2$ mixture, CO_2 gas, isobutane, isobutane-based TE gas, methane, methane-based TE gas, propane and propane-based TE gas. The $r_{m,g}$ calculations required initial spectral fluences of ^1H, ^2H, ^3H, ^3He and ^4He ions released by neutron reactions in the walls, and these were calculated with the Los Alamos High Energy Transport code. Mass stopping powers data were taken from Ziegler *et al.* Additional calculations were made for a few cases in order to test the sensitivity of $r_{m,g}$ to ion production and mass stopping power input data from other sources. The ALICE nuclear reaction code and the recent ICRU stopping power tabulations were used for these tests.

Above 25 MeV, results show $r_{m,g}$ to be a smooth function of neutron energy which approaches the mass stopping power ratios of minimum ionizing particles. A slight energy dependence in $r_{m,g}$ was found below 100 MeV neutron energy. Uncertainties are less than five percent at neutron energies below 100 MeV.

Contents

1 Introduction

Accurate neutron dosimetric measurements are needed for cancer therapy, radiation biology research, radiation damage studies and radiation protection. Absorbed dose from neutrons is frequently deduced from measurements made with cavity ionization detectors. If the cavity and wall are of different materials, Fano's theorem [1] is not applicable and absorbed doses in the gas and wall are not equal. Gas-to-wall absorbed dose conversion factors $r_{m,g}$ convert absorbed dose in a cavity to that in a surrounding wall. The latter is usually the material of interest, therefore the accurate $r_{m,g}$ are needed.

Below 25 MeV, a considerable number of investigations have been reported including those of Makarewicz and Pszona [2], Pszona and Makarewicz [3], Bichsel and Rubach[4], Rubach and Bichsel [5, 6, 7, 8], Siebert and Coyne [9], Bühler et al. [10], Makarewicz et al. [11], Burger and Makarwicz [12], Menzel et al. [13], Pihet and Menzel [14] and Pihet [15]. Above 25 MeV, values for a few gas-wall combinations were reported by Menzel et al. [13], Hartmann et al. [16, 17], Pihet et al. [15] and Binns et al. [18]. The latter are limited to a few gas-wall combinations and have large uncertainties.

The aim of this work is to provide accurate $r_{m,g}$ values above 25 MeV. Values of $r_{m,g}$ were calculated with the Bragg Gray (B-G) cavity theory, i.e., for infinitesimal cavities, in the 25 to 250 MeV neutron energy range. Wall materials investigated include C, O, Mg, Al, Si, Fe, Zr, AlN, Al_2O_3, SiO_2, ZrO_2 and A-150 tissue-equivalent plastic; gases include acetylene, dry air, Ar, an Ar-CO_2 mixture, CO_2, isobutane, isobutane-based tissue-equivalent (ITE) gas, methane, methane-based tissue-equivalent (MTE) gas, propane and propane-based tissue-equivalent (PTE) gas. In addition, various sensitivity tests were made in order to bound the uncertainties.

2 Methods

The gas-to-wall absorbed dose conversion factor is defined as

$$r_{m,g} = \frac{\sum_i D_i^m}{\sum_i D_i^g}.$$

(1)

where D_i^m and D_i^g denote the absorbed doses in the wall and gas. respectively, and i indicates ion species. In the present work, differences in mass stopping powers and atomic compositions are considered, but perturbation of the primary neutron fluence in the wall is not. Energy deposition is considered for Coulomb interactions of secondary charged particles produced by primary neutron interactions but not for nuclear de-excitation and radiative processes.

In an infinitesimal volume element near the gas-wall interface the absorbed dose is given by

$$D^k = \int_0^\cdot \Phi_E^i \cdot (S/\rho)_i^k \, dE.$$ (2)

where k denotes either the gas g or wall m material. Φ_E^i the ion spectral fluence, $(S/\rho)_i^k$ the corresponding mass stopping power, and E the ion energy. Integration over ion energy denotes application of the continuous slowing-down approximation.

In general, ions generated in the wall lose some energy before reaching the gas-wall interface. On the assumption that charged particle equilibrium (CPE) exists at the gas-wall interface, the spectral fluence at the interface Φ_E^i is

$$\Phi_E^i = \frac{1}{(S/\rho)_i} \int_E^{E_{max}} N_{E'}^i \, dE'.$$ (3)

where N_E^i denotes the number of ions of species i of ion energy E released in the wall per unit mass of wall [19]. or

$$N_E^i = n \, \Phi^n \, \sigma_E^i$$ (4)

where Φ^n is the neutron fluence. σ_E^i the differential cross section for producing an ion of the ith species with energy E. and n the number of target nuclei per unit wall mass. Φ_E^i is commonly called the slowing down spectral fluence.

A variety of particles are produced from neutron interactions. Elastic and inelastic scattering of neutrons produce recoil nuclei, and nonelastic reactions can produce light ions such as ^{1}H and ^{4}He as well as heavier ions. Given the scarcity of charged particle production cross sections in the 25 to 250 MeV neutron energy region for the wall materials under consideration. nuclear model calculations were used to predict charged particle production in the walls. The Los Alamos High Energy Transport Code (LAHET) code [20] was used to

calculate N_E^i values except for ions of atomic mass number $A > 4$, hereafter referred to as heavy-recoil (HR) ions. In addition to recoil nuclei, HR ions arise from nuclear reactions. Above 25 MeV, the lack of a precise knowledge of the reaction mechanisms make it difficult to accurately calculate HR spectral fluences. Romero *et al.* [21] estimated the kerma from elastic and nonelastic reactions for several light nuclei including C, N and O at neutron energies between 27 and 61 MeV. In each case, the fraction of nonelastic recoil kerma was larger than that from elastic recoil kerma. They reported about 50 percent uncertainty for their estimates of nonelastic recoil kerma. Since LAHET does not readily provide spectral fluences of HR ions, we used the following simple approach to estimate them. HR ions were assumed to arise from elastic scattering which is isotropic in the center of mass frame, yielding a constant energy distribution of recoil nuclei N_E^{HR} in the lab frame extending up to the maximum energy kinematically possible. This approach is perhaps not entirely realistic but does, in a sytematic way, yield HR spectra with increasing mean ion energies as the neutron energy is raised. The consequences of this simplification are discussed latter in this paper.

For compound wall materials, the HRs were taken to have the atomic mass number of the most abundant isotope in the compound. The fraction of absorbed dose in the wall from HRs d_m^{HR} was estimated from LAHET energy deposition simulations of spherical shell walls 0.127 cm thick and with an inside diameter of 1.27 cm. In these simulations, light ions were transported but HRs deposited all their kinetic energy at the point of production. Eq. (1) may be expressed as

$$r_{m,g} = \frac{r_{m,g}^L}{(1 - d_m^{HR}) + d_m^{HR} \frac{r_{m,g}^L}{r_{m,g}^{HR}}}, \tag{5}$$

where $r_{m,g}^L$ denotes the mean gas-to-wall absorbed dose conversion factor for ions of $A \leq 4$ which was calculated with Eqs. (1)-(4). Separate gas-to-wall conversion factors for the HRs $r_{m,g}^{HR}$ were calculated with Eqs. (1)-(3). The overall $r_{m,g}$ values were calculated with Eq. (5).

3 Spectral Fluence Calculations

The LAHET code [20] was used to calculate production of ^{1}H, ^{2}H, ^{3}H, ^{3}He, and ^{4}He ions in the wall materials. Slowing-down spectral fluences in C were also calculated based on

differential charged particle production cross sections from the ALICE code [22] in order to estimate the sensitivity of $r_{n,g}$ to N_E^i values from different nuclear models.

Nuclear reactions induced by energetic neutrons may lead to the emission of particles by direct interactions, by the evaporation of particles during or after the formation of a compound nucleus, or by a combination of both. Direct reactions occur when a projectile interacts with only one or possibly a few of the nucleons in a nucleus, and become the predominant initial interaction above about 100 MeV neutron energy. In compound nucleus formation, the excitation energy is distributed evenly amongst the nucleons. Above about 15 MeV neutron energy, particles may be emitted before equilibration of the nucleus occurs and is termed precompound emission. For each of these processes LAHET includes models that are briefly described here.

The intranuclear cascade model of Bertini [23] predicts the nucleon emission from direct processes. In this model, particle-particle collisions within the nucleus are made, assuming that the kinematics are not influenced by neighboring nucleons. Spatial variations in nucleon number density, energy, and potential within the nucleus are taken into account. Experimental free-particle cross sections are used to track nucleons within the nucleus. The model is best suited to high neutron energies. LAHET's default low-energy cutoff for this model is 20 MeV neutron energy.

A statistical evaporation model predicts the emission of light ions ($A \leq 4$) from compound nuclei of atomic mass number ($A \geq 17$). The Fermi breakup model [24, 25, 26] is employed for the light nuclei ($A < 17$), in which the de-excitation proceeds with simultaneous breakup of the nuclei into two or more products. Unstable products may also subsequently breakup. LAHET's implementation allows two or three breakup products in an exit channel.

At intermediate neutron energies where neither direct processes nor compound nucleus formation predominate, a single-stage pre-equilibrium model was used. Elastic scattering was treated up to a maximum neutron energy of 50 MeV with the LAHET default elastic scattering cross sections, which were generated with optical model calculations.

Secondary ions of energies near those of the maximum stopping powers are of interest since the stopping powers are less well known and are strong functions of ion energy in this

region. To predict low-energy particle emission. LAHET approximates quantum mechanical barrier penetration. Neutrons are assumed to be emitted with constant probability from zero up to a cutoff energy equal to twice the mean binding energy. The Coulomb barrier is randomly distributed with a function simulating the transmission probability function. The maximum of the neutron cutoff and the Coulomb barrier is taken for the proton cutoff.

The ALICE code [22] generated emission spectra with models for compound nucleus formation and precompound emission similar to those in LAHET. The ALICE code does not model direct reactions. however.

Only ions produced in interactions with primary neutrons were included in the present spectral fluence calculations. Naturally occurring isotopic abundances were adopted from Ref. [27] for the wall elements. The composition of A-150 plastic [28] is given in Table 1.

4   Mass Stopping Powers

Slowing-down spectral fluences were calculated with mass stopping powers from the TRIM program of Ziegler and Biersack [29, 30]. Stopping powers of ^{1}H. ^{4}He and HR ions were taken directly from TRIM. Values for ^{2}H and ^{3}H were obtained by mass scaling of ^{1}H stopping powers and ^{3}He values were similarly obtained from ^{4}He stopping powers. For C and PTE gas, slowing-down spectral fluences and $r_{m,g}$ values were also calculated with the ICRU stopping power tabulations [31]. For materials containing two or more constituents. elemental stopping powers were combined with the Bragg additivity rule. except for the ICRU tabulation for PTE which was assembled with the Bragg additivity rule from propane. CO_2 and N mass stopping powers [31].

Several special gases used in low-pressure proportional counters and ionization chambers for radiation therapy dosimetry or research include TE mixtures that are based on methane [32]. propane [33] and isobutane [34]. and are given in Table 1. Our Ar-CO_2 mixture comprised 95 percent Ar by partial pressure corresponding to mass fractions of 94.5 percent Ar. 1.5 percent C. and 4.0 percent O. and is similar to a mixture described in Ref. [35].

While $r_{m,g}^i$ depends on ratios of mass stopping powers which are weighted with slowing-

down spectral fluences, it is also worthwhile to examine unweighted ratios of wall and gas mass stopping powers $s_{m,g}^i$. These ratios are nearly constant at ion velocities that are well above those of the orbital electrons, and vary more strongly near those energies. In the 10 to 200 keV ion energy range, $s_{m,g}^i$ values from ICRU and TRIM are in substantially good agreement except in some cases at low energies. For example, comparing the $s_{m,g}^i$ values for C and PTE shown in Figs. 4-5, poor agreement is found below one MeV and is suggestive of higher uncertainties in $s_{m,g}^i$ at low ion energies.

5 Results and Discussion

Ion production and slowing-down spectral fluences of ^{1}H and ^{4}He ions in C appear in Figs. 1-2. Absorbed dose fractions d_m^i for several ion species including HRs are shown in Fig. 3.

Tables 2-12 and Figs. 6-16 give the values of $r_{m,g}$ which were calculated with slowing-down spectral fluences based on LAHET calculations, mass stopping powers from TRIM, and which include treatment of HRs. Above about 70 MeV neutron energy $r_{m,g}$ curves are nearly constant because slowing down spectral fluences comprise mainly ions of high energy, where $s_{m,g}^i$ values are almost constant. Below 70 MeV neutron energy, slight variations with energy are observed for most gas-wall combinations and are attributable to the transition towards higher mean ion energies in a region where $s_{m,g}^i$ values vary strongly with energy. This trend results from the decreasing importance of the elastic scattering and evaporation processes and the increasing importance of the direct reactions with increasing neutron energy.

There are relatively few $r_{m,g}$ values in the literature at or above 25 MeV neutron energy. Several investigators have deduced $r_{m,g}$ values from measured microdosimetric spectra in graphite-walled, PTE-filled Rossi counters [13, 15, 18]. All values but that of Pihet et $al.$ [15] at 66 MeV agree with the present calculations to within five percent, as shown in Table 13 and Fig. 17. Values reported by Pihet et $al.$ [15] are systematically several percent lower than our calculations.

Pihet and Menzel [14] reported $r_{m,g}$ values for an A-150 plastic-walled Rossi counter filled

with PTE or MTE for neutron energies of 28 to 60 MeV. Pihet *et al.* reported $r_{m,g}$ values for A-150 plastic and PTE gas for the 26 to 66 MeV neutron energy range. These results deviate from unity by 0.5 percent or less and are in good agreement with the present results.

Hartmann *et al.* [16, 17] reported $r_{m,g}$ values in the energy range under consideration which include an Ar-CO_2 mixture similar to that used in this work and walls of C, O, Mg, Si, Zr and ZrO_2. They approximated the initial spectral fluences as monoenergetic and of half the maximum possible energy determined by reaction kinematics. ^{1}H, ^{4}He, HR and perhaps other ions were included in their calculations. Good agreement with the present work is found for the C wall. Table 11 compares Hartmann's values with the present work.

6   Uncertainties

Uncertainties in the $r_{m,g}$ values arise from the mass stopping powers, ion spectral fluences, and simplifications adopted for the treatment of HRs.

To test the sensitivity of $r_{m,g}$ to stopping power input data, several otherwise identical $r_{m,g}^L$ calculations (*i.e.*, $r_{m,g}$ excluding treatment of HRs) were made with stopping powers from either TRIM or ICRU and appear in Fig. 17. Only small systematic differences of 1 to 2 percent in $r_{m,g}^L$ were found. Based on the comparison of several $r_{m,g}^L$ values and the discussion of phase effects from Ref. [31], the total uncertainty in $r_{m,g}$ due to the mass stopping-power data is estimated to be less than four percent.

Sensitivity of $r_{m,g}^L$ to the shape of the ion spectral fluences was tested by comparing otherwise similar $r_{m,g}^L$ calculations for C and PTE with either ALICE or LAHET ion spectral fluences. Values of $r_{m,g}^L$ calculated with spectral fluences from ALICE, which did not include ions from direct reactions, are in agreement within better than two percent with the corresponding $r_{m,g}^L$ values that were based on LAHET and TRIM data. However, since the ALICE-based $r_{m,g}$ values were calculated with stopping powers from Ref. [36], the differences in the $r_{m,g}^L$ values are not due solely to differences in the spectral fluences.

In several wall materials, $r_{m,g}$ values for evaporation particles are also indicative of the sensitivity of $r_{m,g}$ to the shape of the spectral fluences. For example, for the C-PTE combination, $r_{m,g}^i$ values for alpha particles vary by only one percent over the entire neutron

energy range owing to the similarity in shape of ion production from evaporation reactions. For protons from direct reactions and for HRs, the shape of the spectral fluences changes significantly with neutron energy, resulting in variations of $r_{m,g}^i$ of up to several percent from 25 to 250 MeV neutron energy.

Perturbation of the primary neutron field in CPE-dimension walls could be significant. This may be important above about 100 MeV neutron energy, particularly for hydrogenous materials such as A-150 plastic. We have not dealt with this topic.

Uncertainties in $r_{m,g}$ from $r_{m,g}^{HR}$ are due to the approximation of N_E^{HR}, mass stopping powers of the HRs, and the estimates of d_m^{HR}. The $r_{m,g}^{HR}$ values are bounded by the $s_{m,g}^{HR}$ values available. The *maximum possible* error in $r_{m,g}^{HR}$ introduced by N_E^{HR} is therefore bounded by the largest possible difference between $r_{m,g}^{HR}$ and $s_{m,g}^{HR}$. In the case of C-PTE, this could be about six percent at the most. Comparing the limiting cases of $r_{m,g}$ with $r_{m,g}^L$ (*i.e.*, examining the difference with and without the treatment of HRs), bounds for the combined uncertainty in $r_{m,g}$ from N_E^{HR} and d_m^{HR} can be obtained. These two limiting cases differ at 11 percent at the most and typically differ by one to two percent from the true value, which is intermediate and closer to the calculated $r_{m,g}$ values. Finally, a step is observed in several $r_{m,g}$ curves at 50 MeV neutron energy. LAHET's cutoff for elastic scattering, with a maximum size of about one percent for the oxygen-wall values. Uncertainties in $r_{m,g}$ from the $r_{m,g}^{HR}$ are thus estimated to be one percent.

Based on the sensitivity calculations we estimate the uncertainty in the recommended $r_{m,g}$ values to be less than five percent in the 25 to 100-MeV neutron energy range. Uncertainties above 100 MeV are likely to be somewhat higher, though no estimates have been made.

ACKNOWLEDGEMENTS

References

[1] U. Fano. *Note on the Bragg-Gray cavity principle for measuring energy dissipation.* Radiat. Res., **1**:237 240, (1951).

[2] M. Makarewicz and S. Pszona. *Theoretical characteristics of a graphite ionization chamber filled with carbon dioxide.* Nucl. Instr. Meth. **153** 423-428 (1978).

[3] S. Pszona and M. Makarewicz. *Effect of cavity size on the sensitivity of a TE-walled, TE-gas-filled ionization chamber for fast neutrons.* Phys. Med. Biol., **27**(8), 1015–1022 (1982).

[4] H. Bichsel and A. Rubach *Neutron dosimetry with spherical ionization chambers II. Basic physical data.* Phys Med. Biol., **27**(8) 1003 1013 (1982).

[5] A. Rubach and H. Bichsel *Neutron dosimetry with spherical ionization chambers I. Theory of the dose conversion factor $r_{m,g}$ and W_n.* Phys. Med. Biol., **27**(7) 893-904 (1982).

[6] A. Rubach and H. Bichsel *Neutron dosimetry with spherical ionization chambers III. Calculated results for tissue-equivalent chambers.* Phys. Med. Biol., **27**(10) 1231-1243 (1982).

[7] A. Rubach and H. Bichsel *Neutron dosimetry with spherical ionization chambers IV. Neutron sensitivities for C CO₂ and tissue-equivalent chambers.* Phys. Med. Biol., **27**(12) 1445-1463 (1982).

[8] A. Rubach, H. Bichsel, and A. Ito. *Neutron dosimetry with spherical ionization chambers V. Experimental measurements and comparison of calculations of the cavity size dependence of the specific ionization.* Phys. Med. Biol. **28**(8) 913–924 (1983).

[9] B.R. Siebert and J.J. Coyne *Dose conversion factors and W_n values for infinitesimal and infinite tissue-equivalent ion chambers in monoenergetic neutron fields from thermal to 20 MeV.* Radiat. Prot. Dosim., **9**(3) 215 218 (1984).

[10] G. Bühler, H. Menzel, H. Schuhmacher, G. Dietze, and S. Guldbakke. *Neutron kerma factors for magnesium and aluminum measured with low-pressure proportional counters.* Phys. Med. Biol., **31**(6) 601 612 (1986).

[11] M. Makarewicz, G. Burger, and H. Bichsel. *On the stopping power for tissue-equivalent gaseous ionization devices used in neutron dosimetry.* Phys. Med. Biol., **31**(3) 281 -284 (1986).

[12] G. Burger and M. Makarewicz *Average energy to produce an ion pair in gases (W values) and related quantities of relevance in neutron dosimetry.* In Proceedings of an Advisory Group Meeting on Nuclear and Atomic Data for Radiotherapy and Related Radiobiology, held in Rijswijk, Iceland, 1985, Vol. STI/PUB/741, pages 225–238, Vienna (1987).

[13] H.G. Menzel, P. Pihet, K.H. Folkerts, P Dahem, and R.E. Grillmaier. *Dosimetry research using low-pressure proportional counters for neutrons with energies up to 60 MeV.* *Radiat. Prot. Dosim.* **23** 389–392 (1988).

[14] P. Pihet and H.G. Menzel. *Atomic data required in accurate measurements of kerma for neutrons with low-pressure proportional counters.* In *Proceedings of an advisory group meeting on atomic and molecular data for radiotherapy, held in Vienna, Austria, 13-16 June, 1988. IAEA-TEDOC-506.* pages 92–105. Vienna (1989).

[15] P. Pihet, S. Guldbakke, H.G. Menzel, and H. Schuhmacher. *Measurement of kerma factors for carbon and A-150 plastic: Neutron energies from 13.9 to 20.0 MeV.* *Phys. Med. Biol.* **37**(10). 1957–1976 (1992).

[16] C.L. Hartmann. *Measurements of neutron kerma factors at 18, 23, and 25 MeV.* PhD thesis, University of Wisconsin - Madison (1991).

[17] C.L. Hartmann, P.M. DeLuca, Jr., and D.W. Pearson. *Measurement of neutron kerma factors in C, O, and Si at 18, 23, and 25 MeV.* *Radiat. Prot. Dosim.* **94**, 25–30 (1992).

[18] P.J. Binns and J.H. Hough. *Kerma associated with high energy neutrons.* *Radiat. Prot. Dosim.* **52**, 105–109 (1994).

[19] R.S. Caswell and J.J. Coyne. *Interactions of neutrons and secondary charged particles with tissue: Secondary charged particle spectra.* *Radiat. Res.* **52**, 448–470 (1972).

[20] R.E. Prael and H. Lichtenstein. *Users guide to LCS: the LAHET Code System.* LANL Report LA-UR-89-3014. Los Alamos National Laboratory (1989).

[21] J.L. Romero, F.P. Brady, and T.S. Subramanian. *Neutron induced charged particle spectra and kerma from 25 to 60 MeV.* In Proceedings of an International Conference on Nuclear Data for Basic and Applied Science, held in Santa Fe, USA, pages 687–699. Gordon and Breach, New York (1986).

[22] M. Blann and J. Bisplinghoff. UCID 19614. Technical report, Lawrence Livermore National Laboratory (1983).

[23] H.W. Bertini. *Intranuclear-cascade calculation of the secondary nucleon spectra from nucleon-nucleus interactions in the energy range 340 to 2900 MeV and comparison with experiment.* *Phys. Rev.* **188**(4). 1711–1730 (1969).

[24] E. Fermi. *High energy nuclear events.* *Prog. Theor. Phys.,* **5**(4):570–583 (1950).

[25] D.J. Brenner, R.E. Prael, J.F. Dicello, and M. Zaider. *Improved calculations of energy deposition from fast neutrons.* In *Proceedings 4th Symposium on Neutron Dosimetry, held in Munich/Neuherberg, Germany. EUR-7448.* pages 103–112. Commission of the European Communities. Luxemborg (1981).

[26] T.S. Subramanian, J.L. Romero, F.P. Brady, J.W. Watson, D.H. Fitzgerald, R. Garrett, G.A. Needham, J.L. Ullmann, and C.I. Zanelli. *Double differential inclusive hydrogen and helium spectra from neutron induced reactions on carbon at 27.4, 39.7, and 60.7 MeV.* *Phys. Rev.,* **25**(1):521–528 (1980).

[27] A.H. Wapstra and G. Audi. *The 1983 atomic mass evaluation. (i). Atomic mass table.* *Nucl. Phys.* **A**(432). 1–54 (1985).

[28] J.B. Smathers, V.A. Otte, A.R. Smith, P.R. Almond, F.H. Attix, J.J. Spokas, W.M. Quam, and L.J. Goodman. *Composition of A-150 tissue-equivalent plastic.* *Med. Phys.* **4**, 74–77 (1975).

[29] J. Biersack and L. Haggmark. *A Monte Carlo computer program for the transport of energetic ions in amorphous targets.* *Nucl. Instr. Meth.* **174**, 257–269 (1980).

[30] J.F. Ziegler and J.P. Biersack. TRIM-92 - Transport of ions in matter computer program. Obtained through private communication with J.F. Ziegler (1994).

[31] *Stopping powers and ranges for protons and alpha particles. ICRU Report 49.* International Commission on Radiation Units and Measurements, Bethesda (1993).

[32] H.H. Rossi and G. Failla. *Tissue-equivalent ionization chambers.* *Nucleonics* **14**, 32–37 (1956).

[33] D. Srdoc. *Experimental technique of measurement of microscopic energy depositions in irradiated matter using Rossi counters.* *Radiat. Res.* **43**, 302–319 (1970).

[34] U.J. Schrewe, H.J. Brede, and H. Schuhmacher. *The use of microdosimetric detectors combined with time-of-flight techniques.* *Nucl. Instr. Meth.* **A**(229). 226–230 (1990).

[35] P.M. DeLuca, Jr., H.H. Barschall, C.L. Hartmann, and D.W. Pearson. *Corrections to kerma factor measurements made by integral techniques.* *Nucl. Instr. Meth.* **B40/41**, 1279–1281 (1989).

[36] H.H. Andersen and J.F. Ziegler. *Hydrogen, stopping powers and ranges in all elements.* Vol. 3 of The stopping and ranges of ions in matter. J.F. Ziegler. (Ed.). Pergamon, New York (1977).

[37] U.J. Schrewe, H.J. Brede, S. Gerdung, R. Nolte, P. Pihet, P. Schmelzbach, and H. Schuhmacher. *Determination of kerma factors of A-150 plastic and carbon at neutron energies between 45 and 66 MeV.* *Radiat. Prot. Dosim.* **44**, 21–24 (1992).

[38] H. Schuhmacher, H.J. Brede, R. Henneck, A. Kunz, J.P. Meulders, P. Pihet, and U.J. Schrewe. *Measurement of neutron kerma factors for carbon and A-150 plastic at neutron energies of 26.3 and 38.7 MeV.* *Phys. Med. Biol.* **37**, 1265–1281 (1992).

A   Tables

Table 1: Elemental mass fractions of tissue-equivalent (TE) materials.

Substance	Percent Elemental Mass					Reference
	H	C	N	O	Other	
A-150 plastic	10.1	77.6	3.5	5.3	1.8 Ca, 1.7 F	Smathers *et al.* [28]
Methane-based TE	10.2	45.6	3.5	40.7		Rossi and Failla [32]
Propane-based TE	10.3	56.9	3.5	29.3		Srdoc [33]
Isobutane-based TE	10.3	59.3	3.5	27.0		Schrewe *et al.* [34]

Table 2:   Calculated values of $r_{m,g}$ for acetylene cavities and various wall materials.

E_n	$r_{m,g}$											
	C	O	Mg	Al	Si	Fe	Zr	AlN	Al_2O_3	SiO_2	ZrO_2	A-150
MeV												
25	0.853	0.764	0.685	0.640	0.678	0.510	0.450	0.703	0.688	0.716	0.497	1.027
30	0.856	0.775	0.689	0.647	0.684	0.521	0.463	0.710	0.696	0.725	0.507	1.027
35	0.858	0.783	0.694	0.654	0.692	0.530	0.473	0.715	0.704	0.732	0.518	1.027
40	0.861	0.791	0.699	0.658	0.698	0.538	0.479	0.721	0.711	0.738	0.527	1.027
50	0.866	0.800	0.707	0.665	0.707	0.549	0.489	0.729	0.721	0.748	0.545	1.027
60	0.874	0.814	0.722	0.679	0.719	0.562	0.499	0.743	0.738	0.763	0.562	1.026
70	0.877	0.821	0.726	0.684	0.725	0.569	0.503	0.748	0.745	0.761	0.571	1.025
80	0.880	0.827	0.731	0.688	0.729	0.575	0.507	0.752	0.751	0.738	0.579	1.025
90	0.882	0.831	0.735	0.692	0.732	0.580	0.511	0.755	0.756	0.780	0.585	1.025
100	0.884	0.835	0.738	0.695	0.736	0.583	0.514	0.758	0.760	0.784	0.590	1.025
125	0.887	0.841	0.745	0.702	0.743	0.593	0.522	0.764	0.768	0.791	0.600	1.024
150	0.890	0.845	0.751	0.708	0.748	0.599	0.528	0.769	0.774	0.797	0.607	1.024
175	0.892	0.848	0.756	0.713	0.753	0.605	0.534	0.773	0.778	0.800	0.613	1.024
200	0.893	0.851	0.759	0.717	0.756	0.609	0.538	0.777	0.782	0.804	0.617	1.024
225	0.894	0.853	0.763	0.720	0.759	0.613	0.541	0.780	0.785	0.807	0.620	1.024
250	0.895	0.855	0.766	0.724	0.761	0.617	0.544	0.782	0.788	0.809	0.623	1.024

Table 3: Calculated values of $r_{m.g}$ for air cavities and various wall materials.

E_n												$r_{m.g}$
	C	O	Mg	Al	Si	Fe	Zr	AlN	Al_2O_3	SiO_2	ZrO_2	A-150
MeV												
25	1.042	0.948	0.848	0.787	0.831	0.617	0.540	0.864	0.856	0.892	0.612	1.214
30	1.041	0.952	0.846	0.789	0.834	0.626	0.552	0.866	0.858	0.894	0.621	1.211
35	1.040	0.956	0.846	0.792	0.839	0.634	0.561	0.867	0.862	0.897	0.630	1.210
40	1.039	0.959	0.847	0.794	0.842	0.641	0.567	0.869	0.865	0.901	0.639	1.209
50	1.037	0.962	0.850	0.796	0.847	0.650	0.576	0.872	0.869	0.906	0.655	1.204
60	1.035	0.968	0.857	0.804	0.852	0.662	0.585	0.878	0.878	0.912	0.669	1.196
70	1.033	0.971	0.859	0.807	0.856	0.668	0.589	0.880	0.882	0.915	0.677	1.193
80	1.032	0.973	0.861	0.809	0.858	0.674	0.593	0.882	0.885	0.918	0.683	1.190
90	1.031	0.974	0.863	0.812	0.860	0.678	0.597	0.883	0.888	0.920	0.689	1.187
100	1.030	0.976	0.865	0.814	0.862	0.682	0.600	0.885	0.890	0.922	0.693	1.185
125	1.029	0.978	0.870	0.819	0.866	0.691	0.608	0.889	0.894	0.925	0.702	1.180
150	1.027	0.980	0.874	0.823	0.869	0.697	0.614	0.892	0.898	0.928	0.708	1.176
175	1.026	0.981	0.877	0.827	0.872	0.703	0.619	0.894	0.901	0.930	0.713	1.174
200	1.026	0.982	0.880	0.830	0.875	0.707	0.624	0.896	0.903	0.932	0.717	1.172
225	1.025	0.983	0.882	0.833	0.877	0.710	0.627	0.898	0.905	0.933	0.720	1.170
250	1.025	0.983	0.885	0.836	0.878	0.713	0.629	0.900	0.907	0.935	0.723	1.168

Table 4: Calculated values of $r_{m.g}$ for Ar cavities and various wall materials.

E_n												$r_{m.g}$
	C	O	Mg	Al	Si	Fe	Zr	AlN	Al_2O_3	SiO_2	ZrO_2	A-150
MeV												
25	1.539	1.408	1.243	1.137	1.203	0.874	0.742	1.251	1.268	1.326	0.886	1.670
30	1.525	1.401	1.222	1.122	1.194	0.878	0.752	1.234	1.253	1.311	0.890	1.657
35	1.513	1.393	1.208	1.113	1.187	0.882	0.758	1.222	1.241	1.300	0.894	1.653
40	1.500	1.381	1.197	1.105	1.181	0.885	0.764	1.212	1.231	1.290	0.897	1.650
50	1.471	1.363	1.183	1.096	1.172	0.890	0.771	1.199	1.216	1.273	0.903	1.630
60	1.433	1.343	1.172	1.090	1.160	0.895	0.777	1.187	1.203	1.255	0.908	1.599
70	1.412	1.332	1.167	1.087	1.156	0.898	0.781	1.182	1.197	1.256	0.912	1.584
80	1.396	1.321	1.163	1.085	1.153	0.901	0.784	1.178	1.192	1.283	0.914	1.571
90	1.383	1.313	1.160	1.084	1.151	0.903	0.787	1.175	1.188	1.235	0.917	1.560
100	1.372	1.306	1.158	1.084	1.149	0.905	0.790	1.173	1.185	1.231	0.919	1.551
125	1.353	1.295	1.155	1.083	1.146	0.910	0.796	1.169	1.180	1.223	0.922	1.530
150	1.339	1.286	1.153	1.083	1.143	0.913	0.800	1.166	1.177	1.218	0.925	1.515
175	1.327	1.279	1.152	1.084	1.142	0.915	0.804	1.164	1.174	1.215	0.927	1.504
200	1.320	1.274	1.151	1.084	1.141	0.917	0.808	1.163	1.173	1.212	0.928	1.495
225	1.313	1.270	1.151	1.085	1.140	0.919	0.810	1.161	1.172	1.209	0.930	1.488
250	1.307	1.267	1.150	1.086	1.140	0.921	0.812	1.160	1.170	1.208	0.931	1.481

Table 5: Calculated values of $r_{m,g}$ for Ar-CO$_2$ cavities and various wall materials.

E_n	$r_{m,g}$											
	C	O	Mg	Al	Si	Fe	Zr	AlN	Al$_2$O$_3$	SiO$_2$	ZrO$_2$	A-150
MeV												
25	1.509	1.385	1.224	1.120	1.184	0.946	0.731	1.232	1.248	1.304	0.872	1.641
30	1.497	1.377	1.204	1.105	1.174	0.931	0.741	1.216	1.232	1.289	0.875	1.630
35	1.486	1.369	1.190	1.096	1.168	0.928	0.747	1.204	1.221	1.278	0.879	1.627
40	1.474	1.359	1.180	1.090	1.163	0.926	0.752	1.194	1.212	1.269	0.882	1.625
50	1.446	1.343	1.166	1.081	1.154	0.924	0.759	1.182	1.198	1.254	0.889	1.606
60	1.409	1.323	1.155	1.075	1.143	0.918	0.765	1.169	1.185	1.236	0.894	1.575
70	1.390	1.313	1.151	1.072	1.139	0.920	0.769	1.164	1.179	1.237	0.898	1.561
80	1.374	1.302	1.147	1.071	1.137	0.923	0.772	1.161	1.175	1.263	0.901	1.549
90	1.363	1.295	1.145	1.070	1.135	0.926	0.776	1.159	1.171	1.217	0.903	1.538
100	1.352	1.289	1.143	1.069	1.133	0.929	0.778	1.157	1.169	1.214	0.905	1.529
125	1.334	1.278	1.141	1.069	1.131	0.934	0.784	1.153	1.164	1.207	0.909	1.510
150	1.321	1.269	1.139	1.070	1.129	0.938	0.789	1.151	1.162	1.203	0.912	1.495
175	1.310	1.264	1.139	1.071	1.128	0.942	0.793	1.150	1.160	1.200	0.915	1.486
200	1.304	1.259	1.138	1.072	1.127	0.945	0.797	1.148	1.158	1.197	0.916	1.477
225	1.297	1.255	1.138	1.073	1.127	0.948	0.799	1.147	1.157	1.195	0.918	1.470
250	1.291	1.252	1.137	1.073	1.126	0.950	0.801	1.147	1.157	1.194	0.919	1.463

Table 6: Calculated values of $r_{m,g}$ for CO$_2$ cavities and various wall materials.

E_n	$r_{m,g}$											
	C	O	Mg	Al	Si	Fe	Zr	AlN	Al$_2$O$_3$	SiO$_2$	ZrO$_2$	A-150
MeV												
25	1.064	0.971	0.864	0.799	0.841	0.620	0.539	0.878	0.872	0.908	0.615	1.226
30	1.062	0.974	0.861	0.800	0.844	0.629	0.552	0.879	0.874	0.910	0.624	1.223
35	1.059	0.976	0.861	0.803	0.849	0.637	0.561	0.880	0.876	0.912	0.633	1.223
40	1.057	0.978	0.862	0.805	0.853	0.645	0.568	0.881	0.879	0.914	0.641	1.222
50	1.052	0.979	0.864	0.807	0.857	0.654	0.577	0.883	0.883	0.919	0.657	1.216
60	1.046	0.982	0.869	0.814	0.861	0.666	0.586	0.887	0.889	0.923	0.671	1.206
70	1.043	0.983	0.871	0.816	0.865	0.672	0.590	0.889	0.893	0.922	0.680	1.201
80	1.041	0.984	0.873	0.819	0.868	0.678	0.595	0.891	0.896	0.910	0.686	1.198
90	1.039	0.985	0.875	0.822	0.869	0.683	0.599	0.893	0.898	0.930	0.692	1.195
100	1.037	0.985	0.876	0.824	0.872	0.687	0.602	0.895	0.900	0.931	0.697	1.192
125	1.035	0.986	0.880	0.828	0.876	0.696	0.611	0.898	0.904	0.934	0.705	1.187
150	1.033	0.987	0.884	0.833	0.879	0.702	0.616	0.901	0.907	0.936	0.712	1.182
175	1.032	0.988	0.886	0.836	0.881	0.708	0.622	0.903	0.910	0.938	0.717	1.180
200	1.031	0.988	0.888	0.839	0.883	0.712	0.627	0.905	0.912	0.939	0.721	1.177
225	1.030	0.988	0.891	0.841	0.885	0.716	0.630	0.906	0.913	0.940	0.724	1.175
250	1.029	0.989	0.893	0.844	0.886	0.719	0.633	0.907	0.915	0.941	0.727	1.173

Table 7: Calculated values of $r_{m,g}$ for isobutane cavities and various wall materials.

E_n	$r_{m,g}$											
MeV	C	O	Mg	Al	Si	Fe	Zr	AlN	Al_2O_3	SiO_2	ZrO_2	A-150
25	0.722	0.642	0.580	0.545	0.578	0.440	0.394	0.598	0.581	0.606	0.428	0.889
30	0.726	0.654	0.585	0.553	0.585	0.451	0.406	0.606	0.590	0.614	0.436	0.890
35	0.730	0.664	0.591	0.560	0.593	0.460	0.414	0.613	0.599	0.623	0.447	0.890
40	0.734	0.672	0.597	0.565	0.600	0.467	0.420	0.619	0.607	0.630	0.456	0.890
50	0.743	0.684	0.606	0.572	0.609	0.477	0.428	0.628	0.618	0.642	0.473	0.892
60	0.755	0.701	0.623	0.588	0.622	0.490	0.438	0.645	0.637	0.660	0.489	0.896
70	0.761	0.709	0.628	0.593	0.629	0.496	0.441	0.650	0.645	0.669	0.498	0.897
80	0.766	0.717	0.633	0.597	0.633	0.502	0.446	0.654	0.652	0.676	0.506	0.898
90	0.770	0.722	0.637	0.601	0.637	0.507	0.449	0.658	0.657	0.682	0.512	0.899
100	0.773	0.727	0.641	0.605	0.641	0.510	0.452	0.661	0.662	0.686	0.517	0.900
125	0.778	0.735	0.649	0.612	0.648	0.519	0.459	0.668	0.671	0.694	0.526	0.902
150	0.783	0.741	0.656	0.618	0.654	0.525	0.464	0.674	0.677	0.701	0.533	0.904
175	0.786	0.745	0.660	0.623	0.659	0.531	0.470	0.678	0.682	0.705	0.539	0.905
200	0.788	0.749	0.665	0.628	0.663	0.535	0.474	0.682	0.686	0.708	0.542	0.906
225	0.790	0.751	0.668	0.631	0.666	0.539	0.477	0.685	0.690	0.712	0.545	0.907
250	0.792	0.754	0.672	0.636	0.668	0.542	0.479	0.688	0.693	0.714	0.548	0.907

Table 8: Calculated values of $r_{m,g}$ for isobutane-based tissue-equivalent gas cavities and various wall materials.

E_n	$r_{m,g}$											
MeV	C	O	Mg	Al	Si	Fe	Zr	AlN	Al_2O_3	SiO_2	ZrO_2	A-150
25	0.830	0.745	0.669	0.626	0.663	0.499	0.442	0.687	0.672	0.700	0.488	1.001
30	0.833	0.755	0.673	0.633	0.668	0.510	0.455	0.694	0.680	0.708	0.497	1.001
35	0.835	0.763	0.677	0.639	0.676	0.519	0.463	0.699	0.688	0.714	0.508	1.001
40	0.838	0.770	0.682	0.643	0.682	0.526	0.470	0.704	0.694	0.721	0.517	1.001
50	0.844	0.779	0.690	0.649	0.690	0.536	0.479	0.712	0.704	0.731	0.534	1.001
60	0.851	0.793	0.704	0.663	0.701	0.549	0.488	0.725	0.720	0.745	0.550	1.001
70	0.855	0.800	0.709	0.667	0.707	0.556	0.492	0.730	0.727	0.743	0.559	1.000
80	0.858	0.806	0.713	0.671	0.712	0.561	0.496	0.734	0.733	0.719	0.567	1.000
90	0.860	0.810	0.716	0.675	0.715	0.566	0.500	0.737	0.738	0.761	0.573	1.000
100	0.863	0.814	0.720	0.678	0.718	0.570	0.503	0.740	0.742	0.765	0.578	1.000
125	0.866	0.820	0.727	0.685	0.725	0.579	0.511	0.746	0.750	0.772	0.587	1.000
150	0.869	0.825	0.733	0.691	0.730	0.585	0.516	0.751	0.755	0.777	0.594	1.000
175	0.871	0.828	0.737	0.695	0.734	0.591	0.522	0.755	0.760	0.781	0.600	1.000
200	0.872	0.831	0.741	0.700	0.738	0.595	0.526	0.758	0.763	0.784	0.603	1.000
225	0.873	0.833	0.744	0.703	0.741	0.599	0.529	0.761	0.766	0.787	0.606	1.000
250	0.874	0.835	0.748	0.707	0.743	0.602	0.531	0.763	0.769	0.789	0.609	1.000

Table 9: Calculated values of $r_{m.g}$ for methane cavities and various wall materials.

E_n	$r_{m.g}$											
	C	O	Mg	Al	Si	Fe	Zr	AlN	Al_2O_3	SiO_2	ZrO_2	A-150
MeV												
25	0.641	0.568	0.516	0.486	0.517	0.396	0.358	0.533	0.516	0.537	0.384	0.802
30	0.646	0.581	0.521	0.495	0.523	0.406	0.368	0.542	0.525	0.547	0.392	0.803
35	0.650	0.590	0.528	0.502	0.532	0.415	0.376	0.549	0.535	0.555	0.402	0.803
40	0.655	0.600	0.533	0.507	0.538	0.422	0.382	0.555	0.543	0.562	0.411	0.804
50	0.666	0.611	0.544	0.514	0.547	0.431	0.389	0.565	0.554	0.574	0.427	0.807
60	0.680	0.630	0.561	0.530	0.561	0.444	0.398	0.582	0.573	0.591	0.443	0.812
70	0.687	0.639	0.566	0.535	0.568	0.450	0.401	0.587	0.582	0.589	0.452	0.814
80	0.693	0.647	0.571	0.540	0.572	0.455	0.405	0.592	0.589	0.562	0.459	0.816
90	0.697	0.653	0.575	0.544	0.576	0.460	0.409	0.595	0.594	0.611	0.465	0.818
100	0.701	0.658	0.580	0.547	0.580	0.463	0.411	0.599	0.599	0.616	0.470	0.820
125	0.708	0.667	0.587	0.555	0.587	0.471	0.418	0.606	0.608	0.624	0.478	0.823
150	0.713	0.673	0.594	0.561	0.593	0.477	0.423	0.612	0.614	0.631	0.485	0.825
175	0.717	0.678	0.599	0.566	0.598	0.483	0.428	0.616	0.620	0.636	0.490	0.827
200	0.720	0.682	0.604	0.570	0.602	0.487	0.432	0.620	0.624	0.640	0.494	0.828
225	0.722	0.685	0.608	0.574	0.606	0.490	0.435	0.624	0.628	0.644	0.497	0.830
250	0.724	0.688	0.612	0.578	0.608	0.493	0.436	0.627	0.631	0.646	0.500	0.831

Table 10: Calculated values of $r_{m.g}$ for methane-based tissue-equivalent gas cavities and various wall materials.

E_n	$r_{m.g}$											
	C	O	Mg	Al	Si	Fe	Zr	AlN	Al_2O_3	SiO_2	ZrO_2	A-150
MeV												
25	0.839	0.754	0.677	0.633	0.670	0.504	0.447	0.695	0.681	0.709	0.494	1.009
30	0.841	0.763	0.680	0.639	0.675	0.514	0.459	0.701	0.688	0.716	0.503	1.008
35	0.843	0.771	0.685	0.645	0.683	0.523	0.467	0.706	0.695	0.722	0.513	1.008
40	0.845	0.778	0.689	0.649	0.689	0.531	0.474	0.711	0.702	0.728	0.522	1.008
50	0.851	0.786	0.696	0.655	0.696	0.541	0.482	0.718	0.711	0.738	0.539	1.008
60	0.858	0.800	0.710	0.669	0.707	0.553	0.492	0.731	0.726	0.751	0.555	1.007
70	0.861	0.806	0.714	0.672	0.713	0.560	0.496	0.735	0.733	0.750	0.564	1.007
80	0.864	0.812	0.718	0.677	0.717	0.565	0.500	0.739	0.739	0.726	0.571	1.006
90	0.866	0.816	0.722	0.680	0.720	0.570	0.504	0.742	0.743	0.767	0.577	1.006
100	0.868	0.819	0.725	0.683	0.724	0.574	0.506	0.745	0.747	0.771	0.582	1.006
125	0.871	0.825	0.732	0.690	0.730	0.583	0.514	0.751	0.754	0.777	0.591	1.006
150	0.874	0.830	0.737	0.695	0.735	0.589	0.520	0.755	0.760	0.782	0.598	1.005
175	0.875	0.833	0.742	0.700	0.739	0.595	0.525	0.759	0.764	0.786	0.604	1.005
200	0.877	0.836	0.745	0.704	0.742	0.599	0.529	0.762	0.768	0.789	0.607	1.005
225	0.878	0.837	0.749	0.707	0.745	0.603	0.533	0.765	0.770	0.792	0.610	1.005
250	0.879	0.839	0.752	0.711	0.747	0.606	0.535	0.767	0.773	0.794	0.613	1.005

Table 11: Calculated values of $r_{m,g}$ for propane cavities and various wall materials.

E_n MeV	$r_{m,g}$											
	C	O	Mg	Al	Si	Fe	Zr	AlN	Al_2O_3	SiO_2	ZrO_2	A-150
25	0.711	0.632	0.571	0.537	0.570	0.435	0.389	0.589	0.572	0.596	0.422	0.877
30	0.715	0.644	0.576	0.545	0.577	0.445	0.401	0.598	0.582	0.605	0.431	0.878
35	0.719	0.654	0.583	0.552	0.585	0.454	0.409	0.604	0.591	0.614	0.441	0.879
40	0.723	0.663	0.588	0.558	0.591	0.461	0.415	0.611	0.598	0.621	0.450	0.879
50	0.732	0.674	0.598	0.564	0.600	0.471	0.423	0.620	0.609	0.633	0.467	0.881
60	0.745	0.692	0.615	0.581	0.614	0.484	0.432	0.636	0.629	0.651	0.483	0.885
70	0.751	0.700	0.620	0.585	0.621	0.490	0.436	0.641	0.637	0.660	0.492	0.886
80	0.756	0.708	0.625	0.590	0.625	0.496	0.440	0.646	0.644	0.667	0.500	0.888
90	0.760	0.713	0.629	0.594	0.629	0.500	0.444	0.649	0.649	0.673	0.506	0.889
100	0.763	0.718	0.633	0.597	0.633	0.504	0.446	0.653	0.654	0.677	0.511	0.890
125	0.769	0.726	0.641	0.605	0.640	0.513	0.454	0.660	0.662	0.686	0.520	0.892
150	0.773	0.732	0.647	0.611	0.646	0.519	0.459	0.665	0.669	0.692	0.527	0.894
175	0.777	0.736	0.652	0.616	0.651	0.524	0.464	0.670	0.674	0.696	0.532	0.895
200	0.779	0.740	0.657	0.620	0.655	0.529	0.468	0.674	0.678	0.700	0.536	0.896
225	0.781	0.742	0.660	0.624	0.658	0.532	0.471	0.677	0.681	0.703	0.539	0.896
250	0.783	0.745	0.664	0.628	0.660	0.535	0.473	0.680	0.684	0.706	0.542	0.897

Table 12: Calculated values of $r_{m,g}$ for propane-based tissue-equivalent gas cavities and various wall materials

E_n MeV	$r_{m,g}$											
	C	O	Mg	Al	Si	Fe	Zr	AlN	Al_2O_3	SiO_2	ZrO_2	A-150
25	0.831	0.745	0.670	0.627	0.663	0.500	0.443	0.688	0.673	0.701	0.489	1.002
30	0.834	0.756	0.673	0.633	0.669	0.510	0.455	0.694	0.681	0.708	0.498	1.002
35	0.836	0.764	0.678	0.639	0.677	0.519	0.464	0.700	0.689	0.715	0.508	1.002
40	0.838	0.771	0.683	0.644	0.683	0.527	0.470	0.705	0.695	0.721	0.517	1.002
50	0.844	0.780	0.691	0.650	0.691	0.537	0.479	0.713	0.704	0.731	0.535	1.001
60	0.852	0.794	0.704	0.664	0.702	0.549	0.488	0.726	0.721	0.745	0.551	1.001
70	0.856	0.800	0.709	0.668	0.708	0.556	0.492	0.730	0.728	0.744	0.560	1.001
80	0.859	0.807	0.713	0.672	0.712	0.562	0.497	0.734	0.734	0.720	0.567	1.001
90	0.861	0.811	0.717	0.675	0.715	0.566	0.501	0.737	0.738	0.762	0.573	1.001
100	0.863	0.814	0.720	0.679	0.719	0.570	0.503	0.740	0.742	0.765	0.578	1.001
125	0.866	0.821	0.727	0.685	0.725	0.579	0.511	0.746	0.750	0.772	0.587	1.000
150	0.869	0.825	0.733	0.691	0.730	0.586	0.516	0.751	0.755	0.777	0.594	1.000
175	0.871	0.828	0.737	0.696	0.735	0.591	0.522	0.755	0.760	0.781	0.600	1.000
200	0.872	0.831	0.741	0.700	0.738	0.596	0.526	0.758	0.763	0.784	0.603	1.000
225	0.873	0.833	0.744	0.703	0.741	0.599	0.530	0.761	0.766	0.787	0.607	1.000
250	0.874	0.835	0.748	0.707	0.743	0.602	0.532	0.763	0.769	0.789	0.610	1.000

Table 13: Measured and calculated values of $r_{m,g}$ for neutrons incident on graphite-walled detectors containing propane-based tissue-equivalent cavities. Values from previous investigations are based on the technique of Menzel et $al.$ [13], which uses the differences in ionization spectra in graphite and A-150 plastic Rossi counters.

E_n MeV	$r_{m,g}$ (Present work)	$r_{m,g}$ (Previous work)	Reference
26.3	0.832 ± 0.04	0.794 ± 0.036	Pihet et $al.$ [15]
27.0	0.832 ± 0.04	0.80	Binns and Hough [18]
27.8	0.833 ± 0.04	0.82 ± 0.05	Pihet and Menzel [14]
27.8	0.833 ± 0.04	0.85	Menzel et $al.$ [13]
37.8	0.838 ± 0.04	0.802 ± 0.045	Pihet et $al.$ [15]
39.7	0.839 ± 0.04	0.83	Menzel et $al.$ [13]
39.7	0.839 ± 0.04	0.84 ± 0.05	Pihet and Menzel [14]
42.0	0.840 ± 0.04	0.80	Binns and Hough [18]
44.5	0.841 ± 0.04	0.798 ± 0.047	Pihet et $al.$ [15]
58.4	0.848 ± 0.04	0.793 ± 0.071	Pihet et $al.$ [15]
60.3	0.849 ± 0.04	0.84	Menzel et $al.$ [13]
60.3	0.849 ± 0.04	0.85 ± 0.05	Pihet and Menzel [14]
63.0	0.851 ± 0.04	0.88	Binns and Hough [18]
66.0	0.851 ± 0.04	0.782 ± 0.120	Pihet et $al.$ [15]

Table 14: Calculated $r_{m,g}$ values for C, Mg, Si, Zr and ZrO_2 walls with Ar-CO_2 cavities.

E_n MeV	Wall	$r_{m,g}$ (Present work)	$r_{m,g}$ (Previous work)	Reference
25	C	1.509 ± 0.07	1.47 ± 0.17	Hartmann [16]
25	Mg	1.224 ± 0.07	1.11 ± 0.13	Hartmann [16]
25	Si	1.184 ± 0.06	1.05 ± 0.12	Hartmann [16]
25	Zr	0.731 ± 0.04	0.510	Hartmann [16]
25	ZrO_2	0.872 ± 0.04	0.674†	Hartmann [16]
25	ZrO_2	0.872 ± 0.04	0.756 ± 0.09‡	Hartmann [16]
25	Fe	0.946 ± 0.05	0.494 ± 0.06	Hartmann [16]

† Only $Zr(n,X)$ reactions were considered.

‡ Only $O(n,X)$ reactions were considered.

Table 15: Calculated and measured $r_{\mathrm{m,g}}$ values for neutrons incident on A-150 plastic counters with propane-based and methane-based tissue-equivalent gases.

E_{n} MeV	$r_{\mathrm{m,g}}$ (Present work)	$r_{\mathrm{m,g}}$ (Previous work)	Gas	Reference
26.3†	1.000 ± 0.05	1.000 ± 0.01	PTE	Pihet *et al.* [15]
37.8†	1.000 ± 0.05	1.000 ± 0.01	PTE	Pihet *et al.* [15]
44.5†	1.000 ± 0.05	1.000 ± 0.01	PTE	Pihet *et al.* [15]
58.4†	1.000 ± 0.05	1.000 ± 0.01	PTE	Pihet *et al.* [15]
66.0†	1.000 ± 0.05	1.000 ± 0.01	PTE	Pihet *et al.* [15]
27.8	1.008 ± 0.05	0.995 ± 0.05	MTE	Pihet and Menzel [14]
37.8	1.008 ± 0.05	0.998 ± 0.05	MTE	Pihet and Menzel [14]
60.3	1.007 ± 0.05	0.997 ± 0.05	MTE	Pihet and Menzel [14]

†Neutron energies corrected from Refs. [37, 38]

B Figures
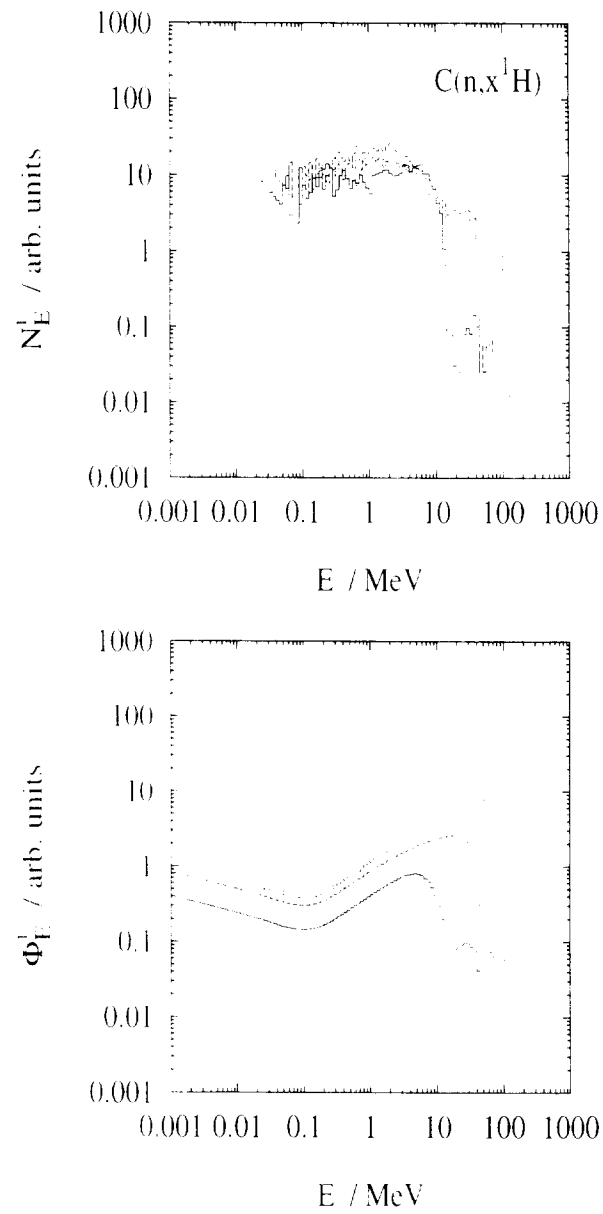
Figure 1: Calculated ion production N_E^i (top) and slowing-down spectral fluences Φ_E^i (bottom) of ^{1}H ions from monoenergetic neutrons incident on ^{nat}C. Slowing-down spectral fluences were calculated assuming CPE conditions at the gas-wall interface. Results for incident neutron energies E_n of 25 MeV (————), 50 MeV (— — —), 100 MeV (— — — —), and 250 MeV ($\cdots$) are shown.
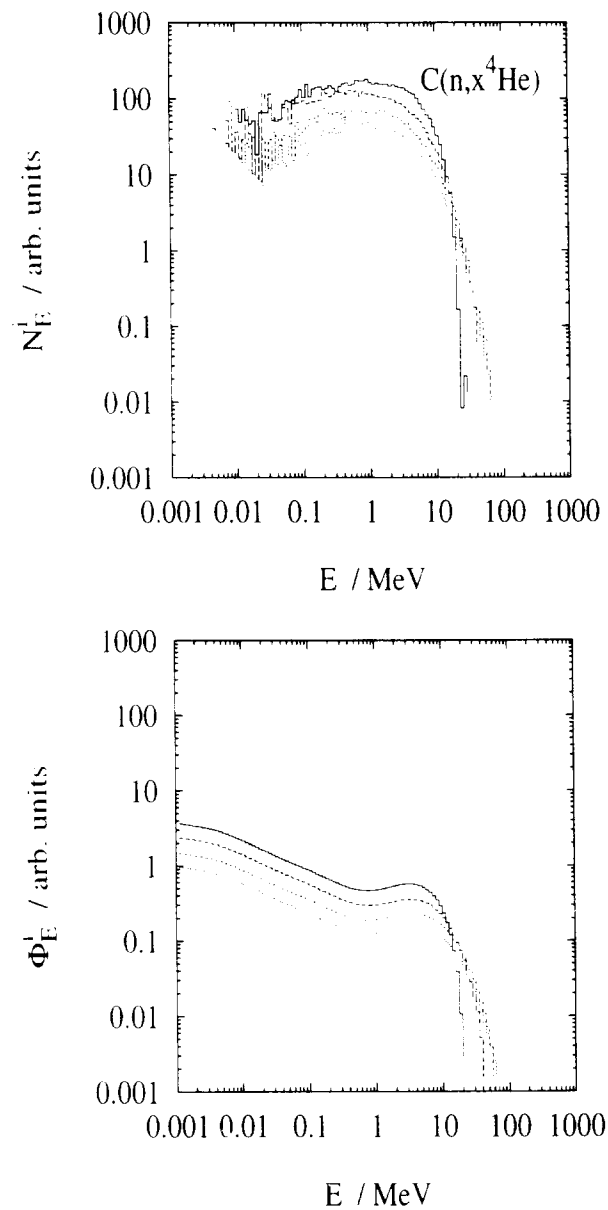
Figure 2: Calculated ion production N_E^i (top) and slowing-down spectral fluences Φ_E^i (bottom) of ⁴He ions from monoenergetic neutrons incident on ^{nat}C. Slowing-down spectral fluences were calculated assuming CPE conditions at the gas-wall interface. Results for incident neutron energies E_n of 25 MeV (————), 50 MeV (— — —), 100 MeV(– – – –), and 250 MeV (⋯) are shown.
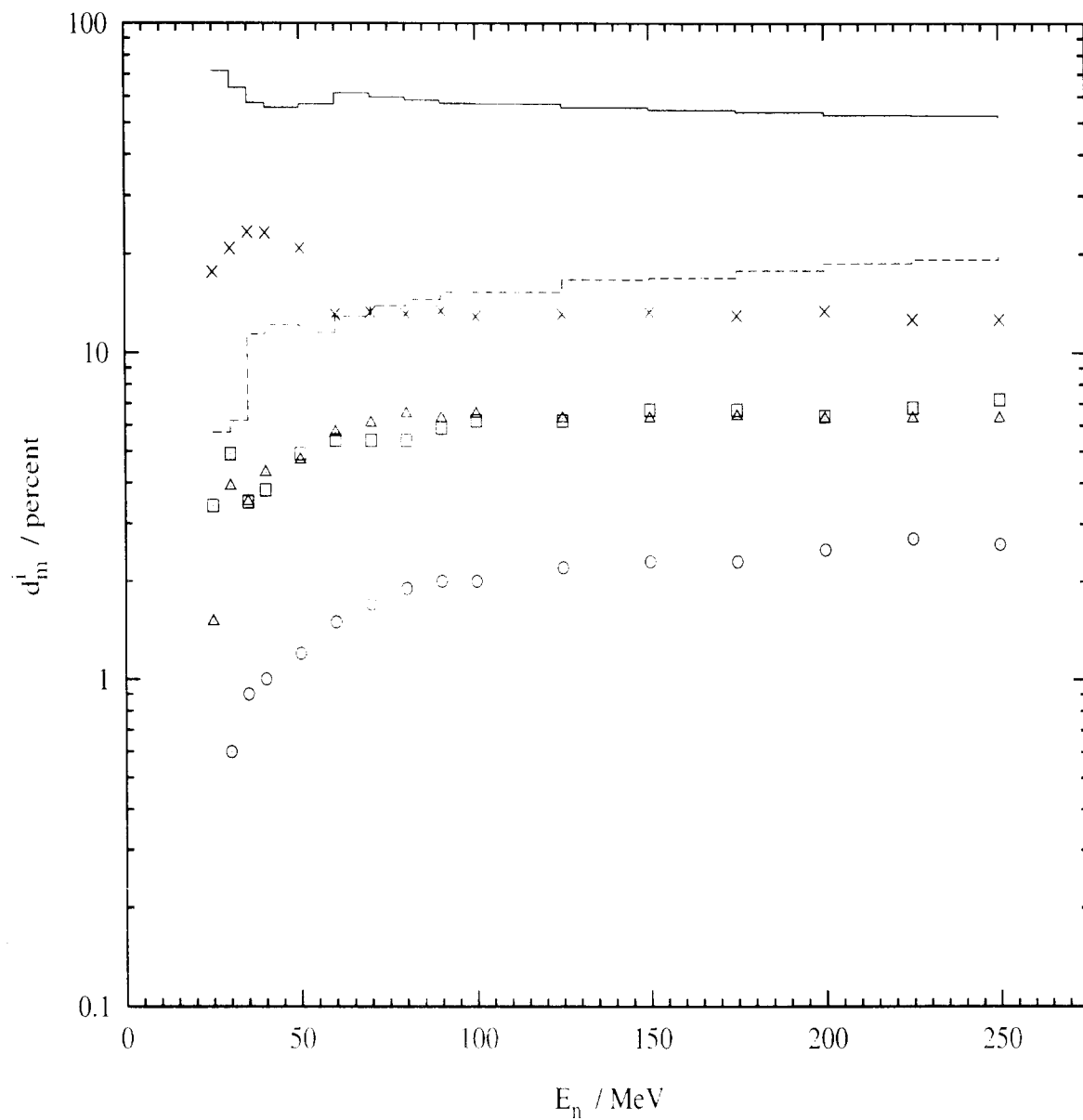
Figure 3: Absorbed doses fractions d_m^i vs. neutron energy E_n in a C wall for ion species i, including ^{1}H (— — — —), ^{2}H ($\square$), ^{3}H ($\triangle$), ^{3}He ($\circ$), ^{4}He (———————), and HR ($\times$) ions. Values were obtained from Monte Carlo transport calculations made with LAHET to simulate a 1.27 mm thick hollow spherical wall
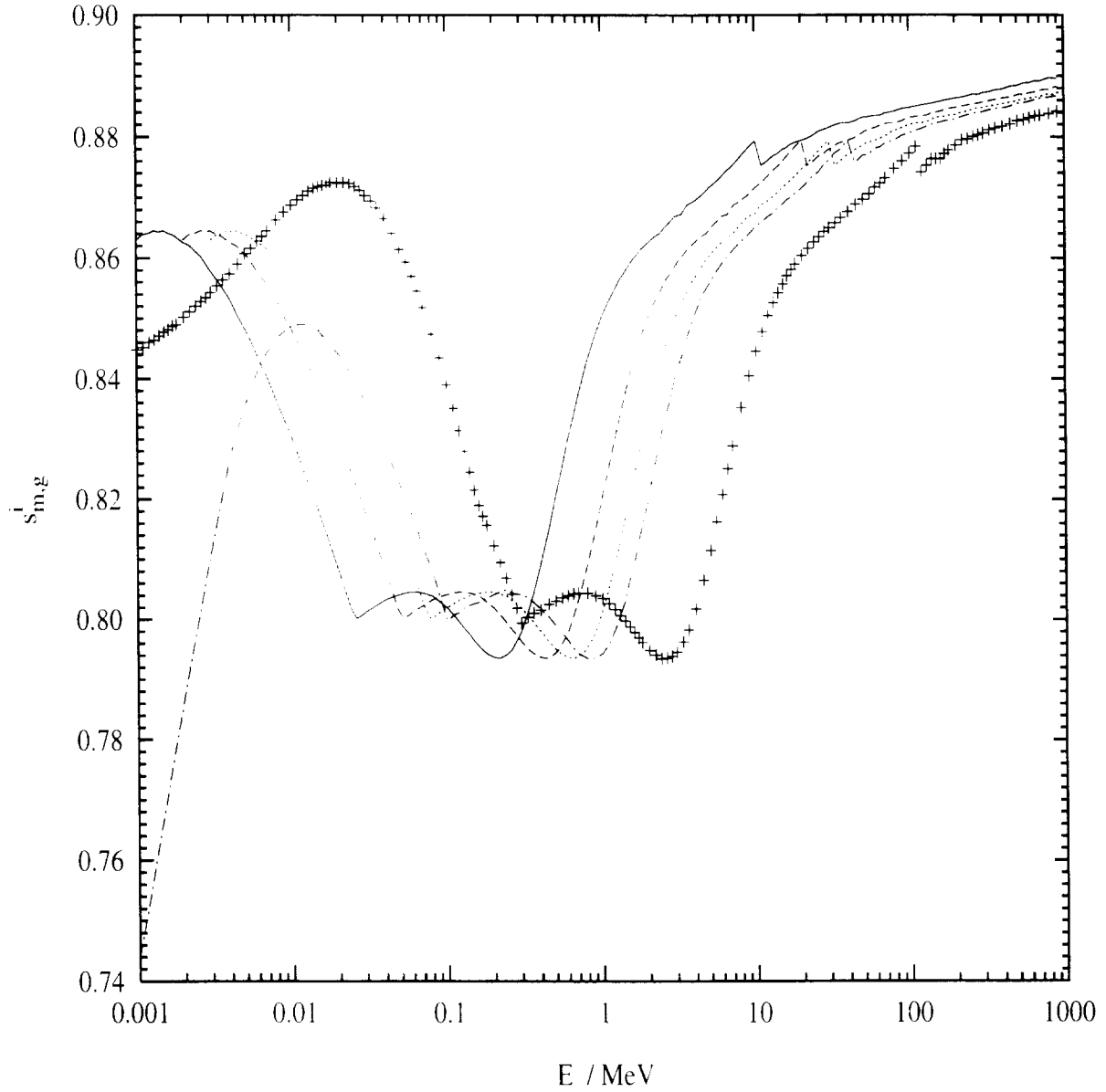
Figure 4: Mass-stopping-power ratios $s^i_{m,g}$ of C to propane-based tissue-equivalent gas for several ion species i vs. ion energy E. Ratios for ^{1}H (———), ^{2}H (— — —), ^{3}H ($\cdots$), ^{4}He (— · — · —), and HR (+) ions are shown. Mass stopping powers are taken from the TRIM code [30].
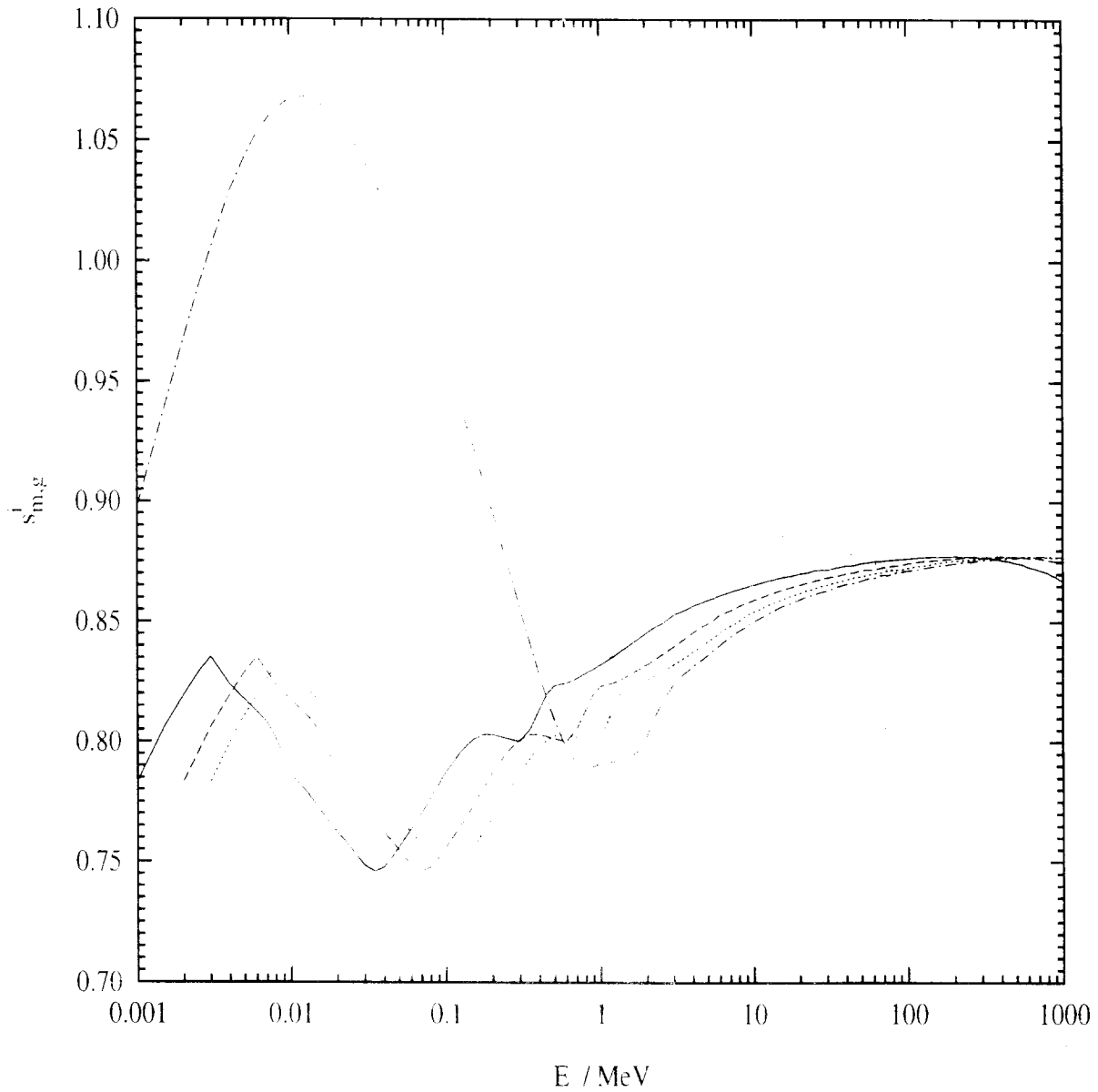
Figure 5: Mass stopping-power ratios $s_{m,g}^i$ of C to propane-based tissue-equivalent gas for several ion species i vs. ion energy E. Ratios for ^{1}H (————), ^{2}H (— — —), ^{3}H (· · ·), and ^{4}He (— · — · —) are shown. Mass-stopping powers are taken from the ICRU [31].
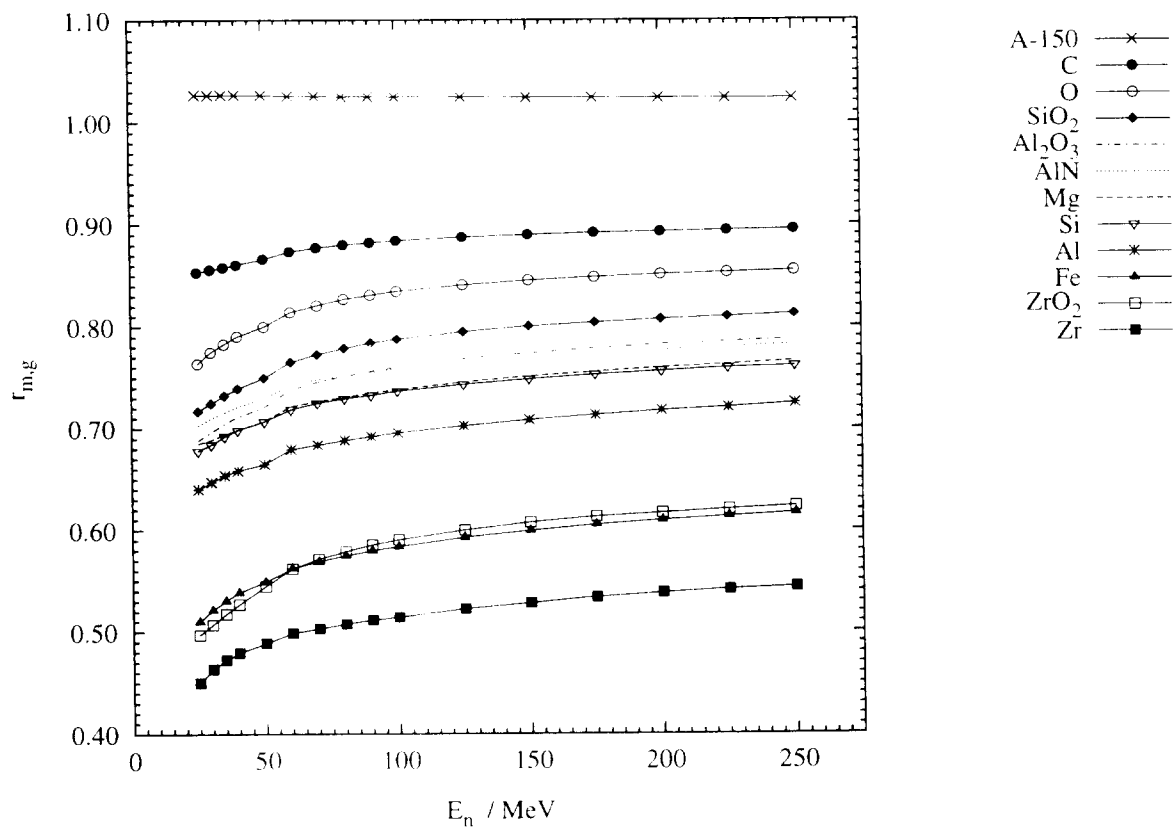
Figure 6: Calculated values of $r_{m,g}$ vs. neutron energy E_n for various wall materials m and acetylene gas g. The $r_{m,g}$ values were calculated with slowing-down spectral fluences based on LAHET calculations, mass stopping powers of TRIM [30], and include treatment of HR ions.
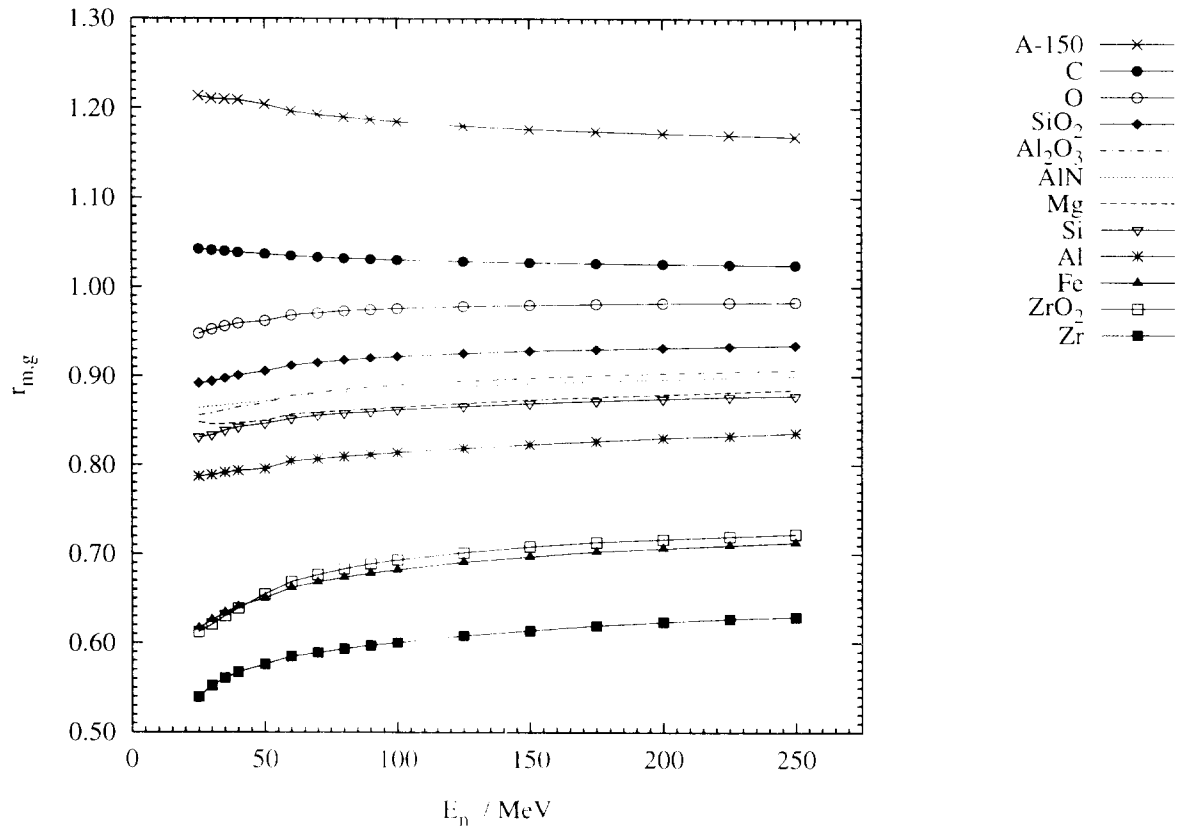
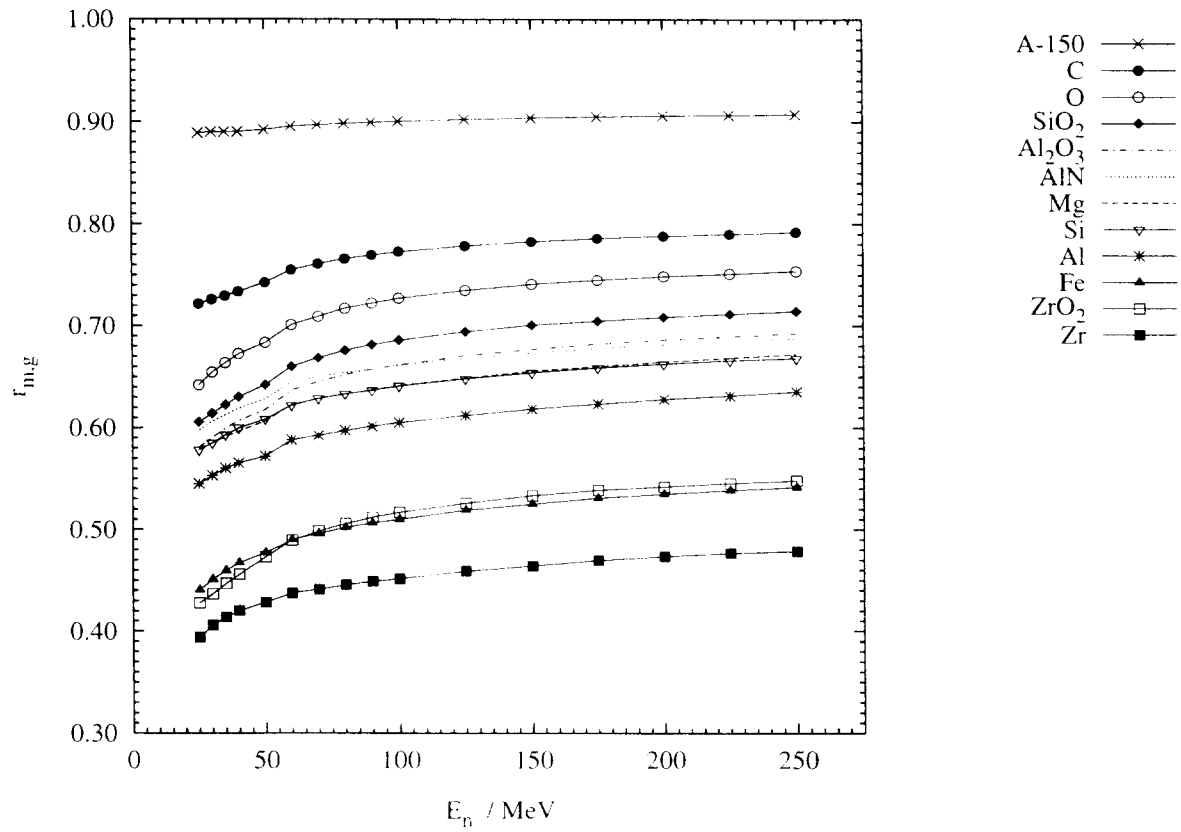Figure 7: Calculated values of $r_{m,g}$ vs. neutron energy E_n for various wall materials m and gas g of dry air. The $r_{m,g}$ values were calculated with slowing-down spectral fluences based on LAHET calculations, mass stopping powers taken from TRIM [30], and include treatment of HR ions.
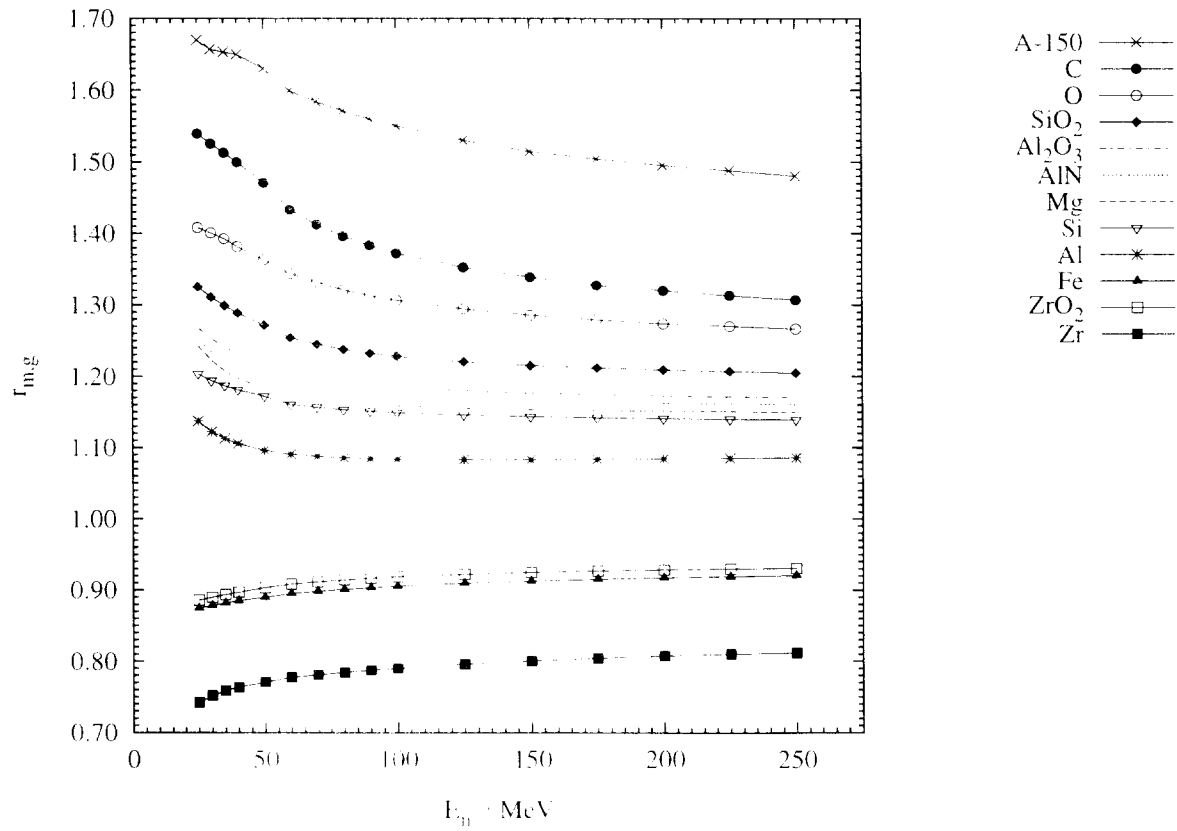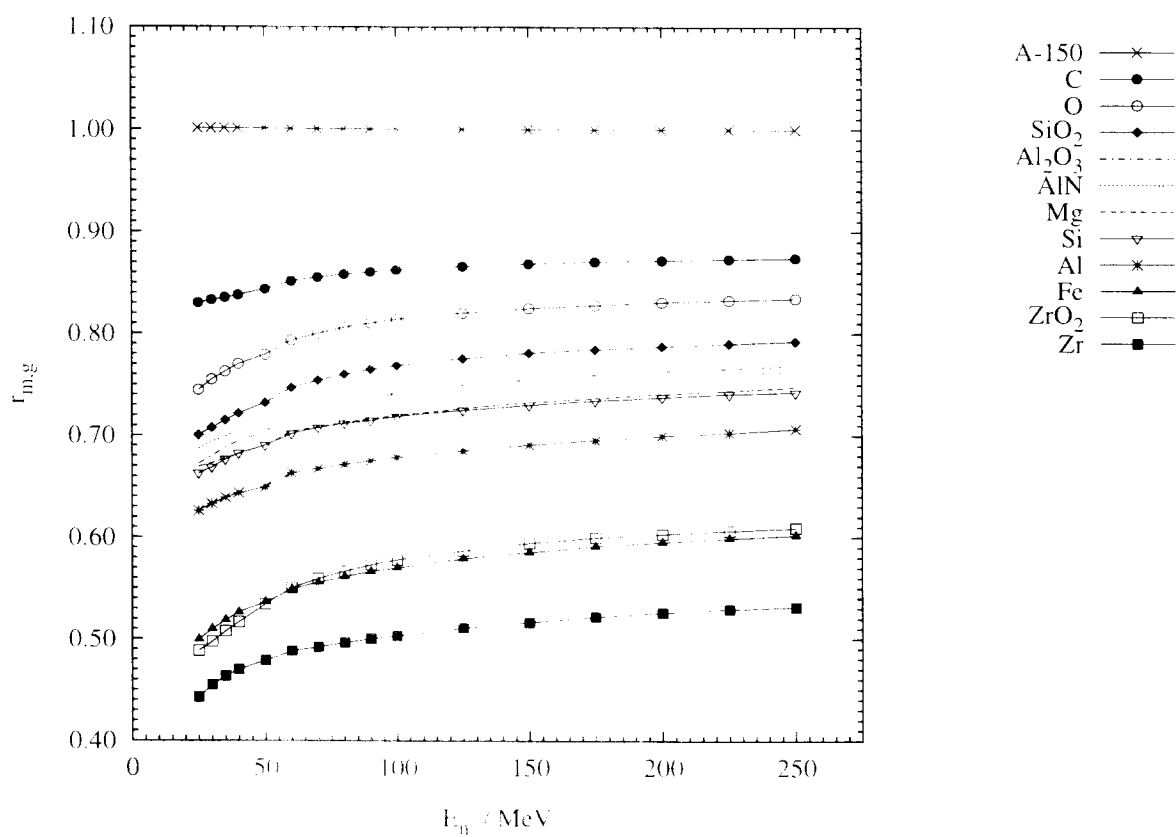
Figure 8: Calculated values of $r_{m,g}$ vs. neutron energy E_n for various wall materials m and Ar gas g. The $r_{m,g}$ values were calculated with slowing-down spectral fluences based on LAHET calculations, mass stopping powers taken from TRIM [30], and include treatment of HR ions.
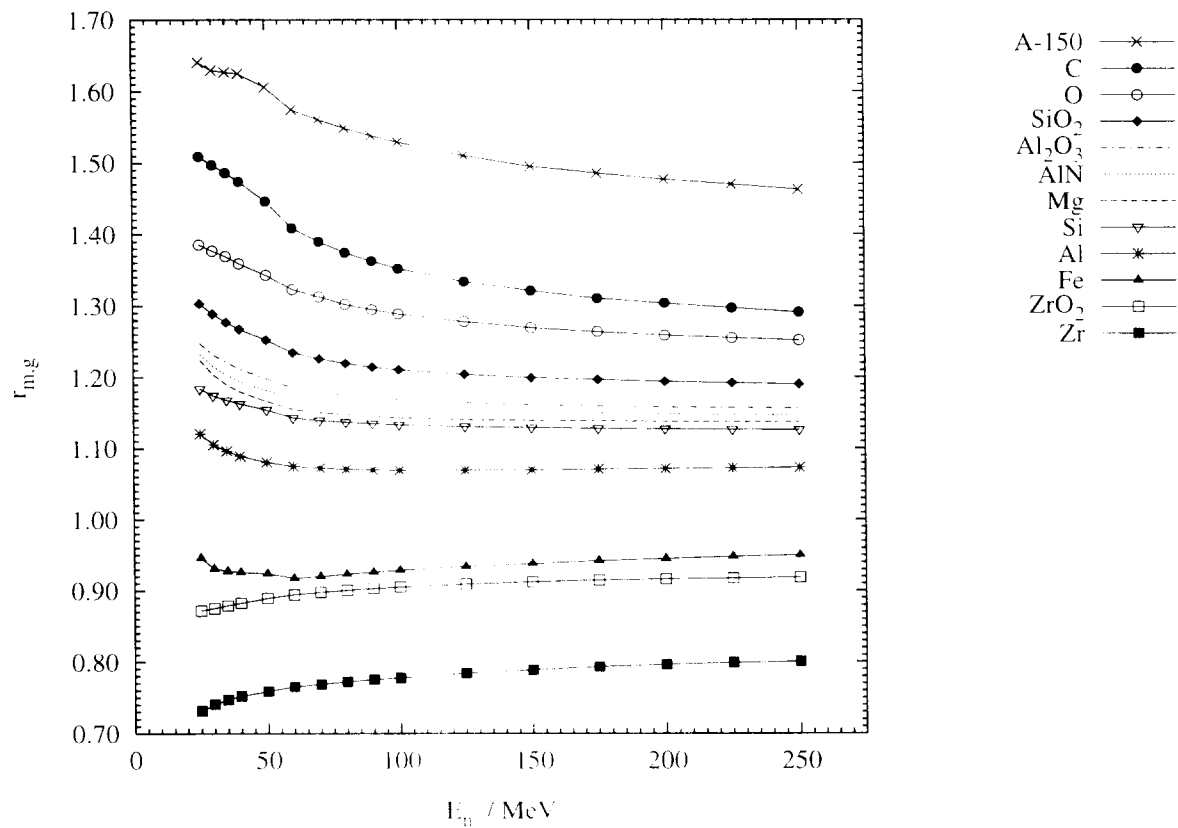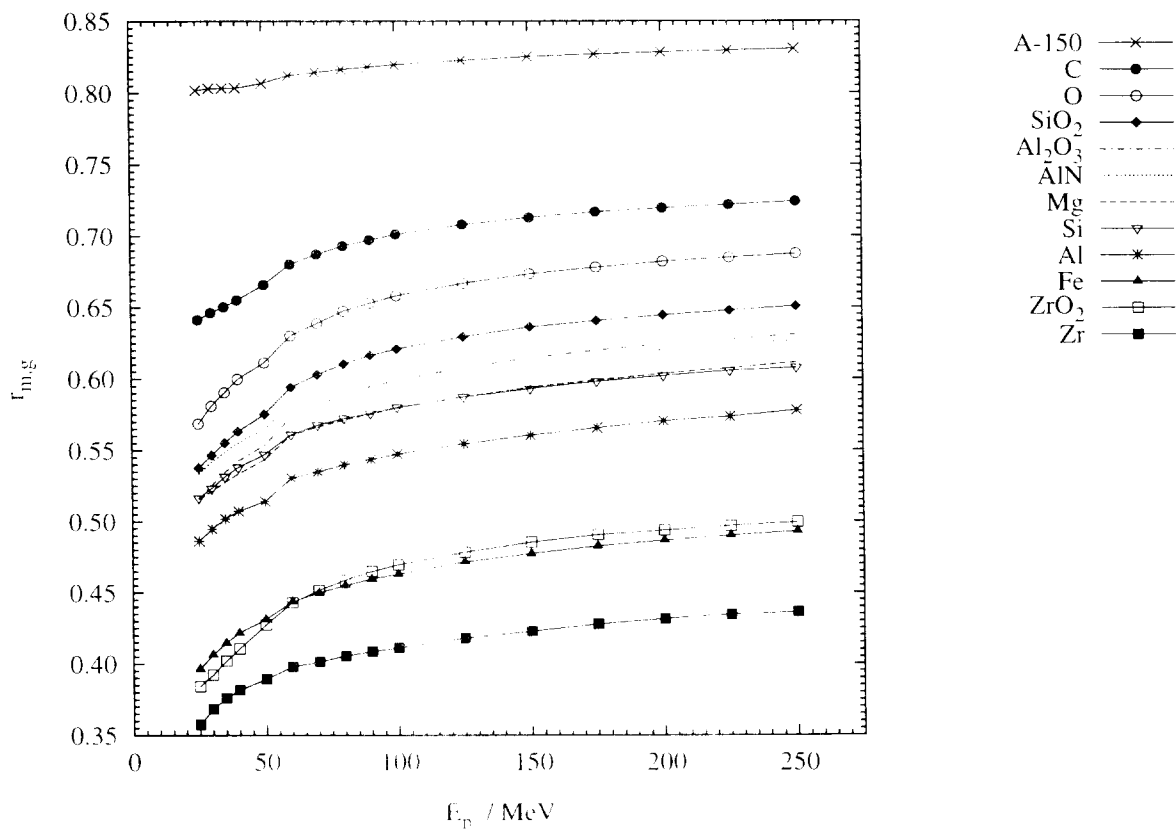
Figure 9: Calculated values of $r_{m,g}$ vs. neutron energy E_n for various wall materials m and Ar-CO_2 gas g. The $r_{m,g}$ values were calculated with slowing-down spectral fluences based on LAHET calculations, mass stopping powers taken from TRIM [30], and include treatment of HR ions.
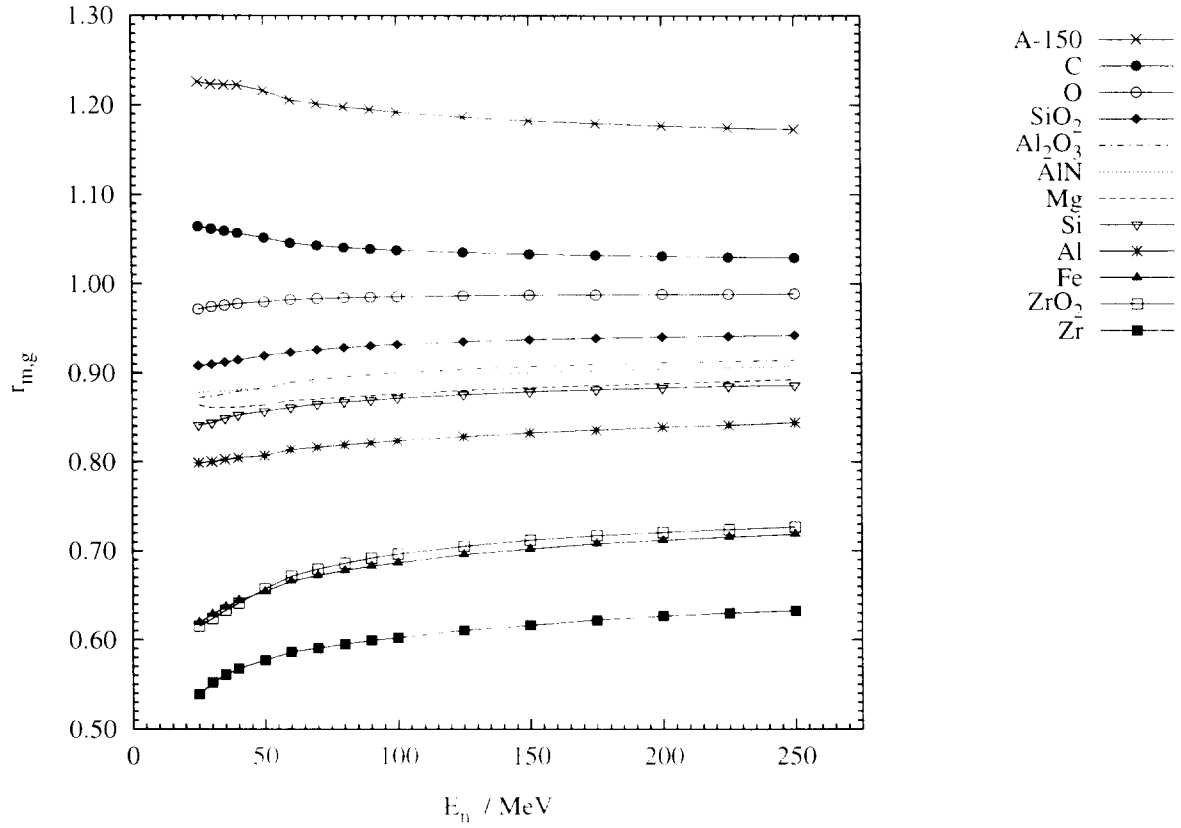
Figure 10: Calculated values of $r_{m,g}$ vs. neutron energy E_n for various wall materials m and CO_2 gas g. The $r_{m,g}$ values were calculated with slowing-down spectral fluences based on LAHET calculations, mass stopping powers taken from TRIM [30]. and include treatment of HR ions.
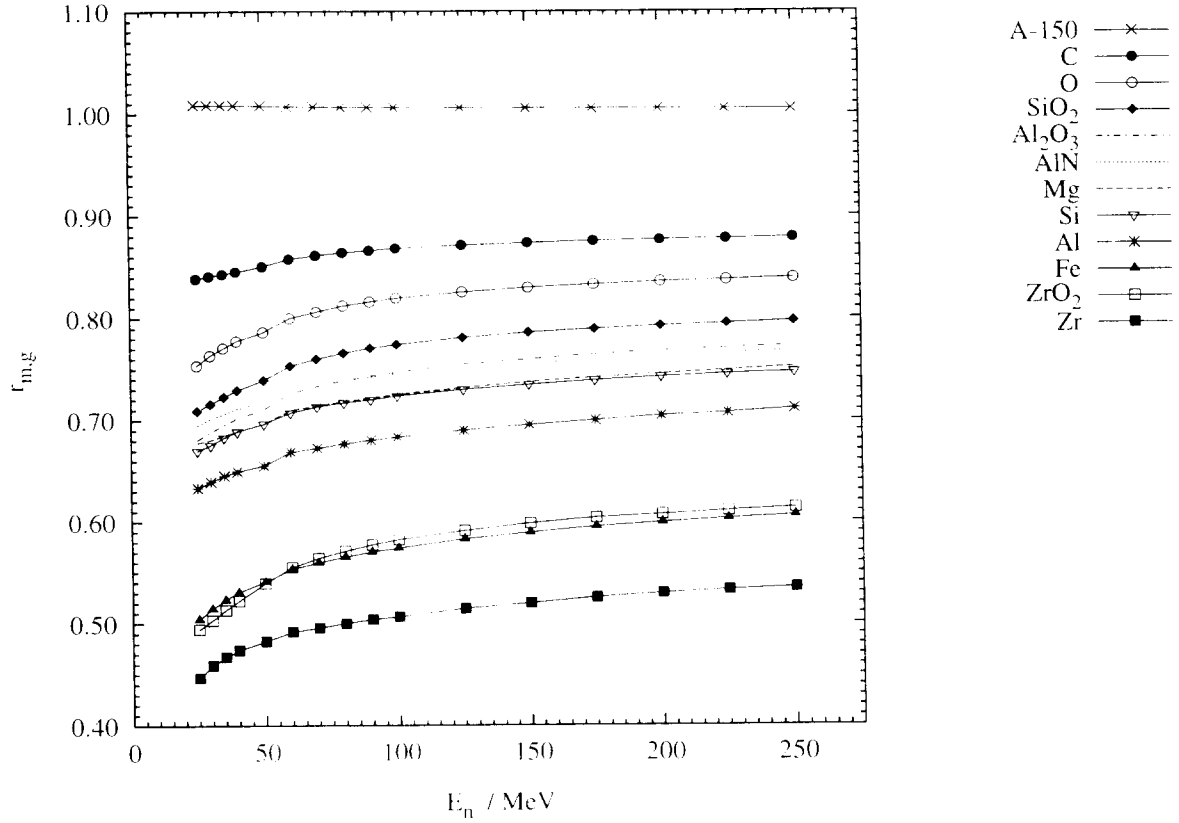
Figure 11: Calculated values of $r_{m,g}$ vs. neutron energy E_n for various wall materials m and isobutane gas g. The $r_{m,g}$ values were calculated with slowing-down spectral fluences based on LAHET calculations, mass stopping powers taken from TRIM [30], and include treatment of HR ions.

Figure 12: Calculated values of $r_{m,g}$ vs. neutron energy E_n for various wall materials m and isobutane-based tisue-equivalent gas g. The $r_{m,g}$ values were calculated with slowing-down spectral fluences based on LAHET calculations, mass stopping powers taken from TRIM [30], and include treatment of HR ions.
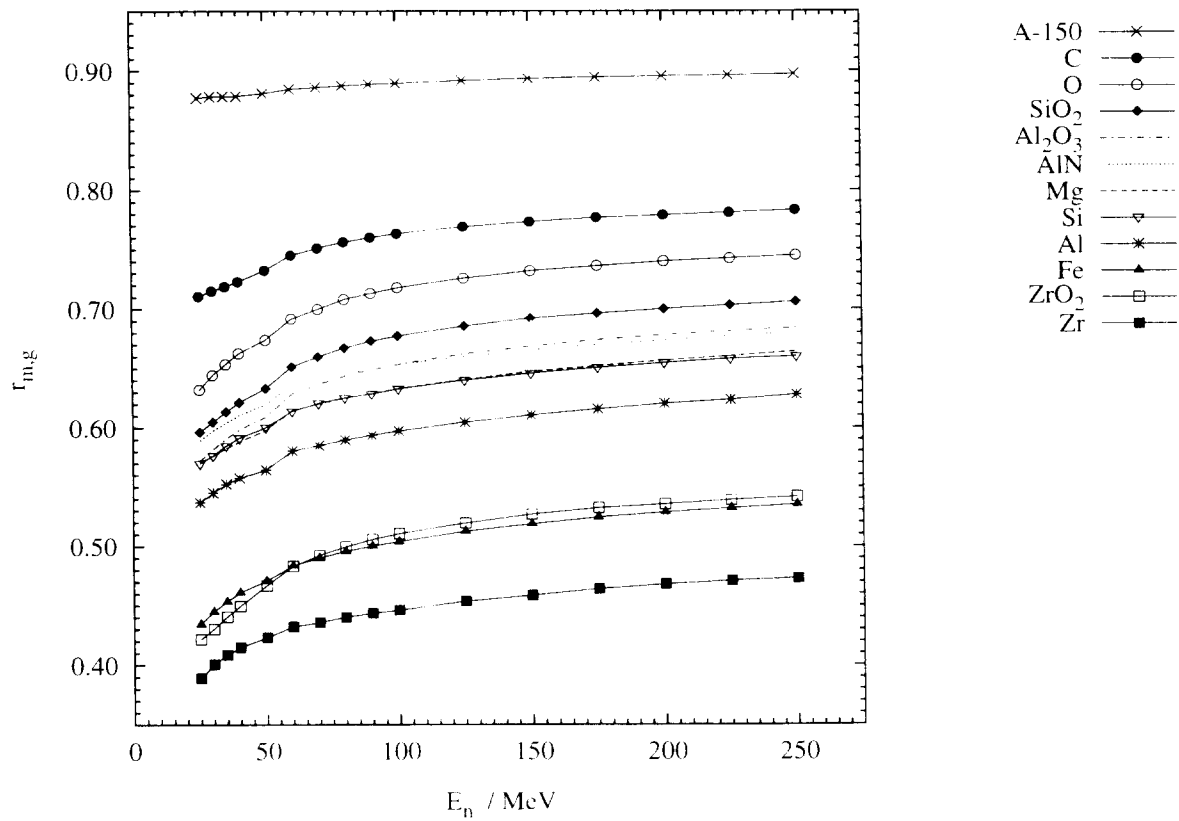
Figure 13: Calculated values of $r_{m,g}$ vs. neutron energy E_n for various wall materials m and methane gas g. The $r_{m,g}$ values were calculated with slowing-down spectral fluences based on LAHET calculations, mass stopping powers taken from TRIM [30], and include treatment of HR ions.
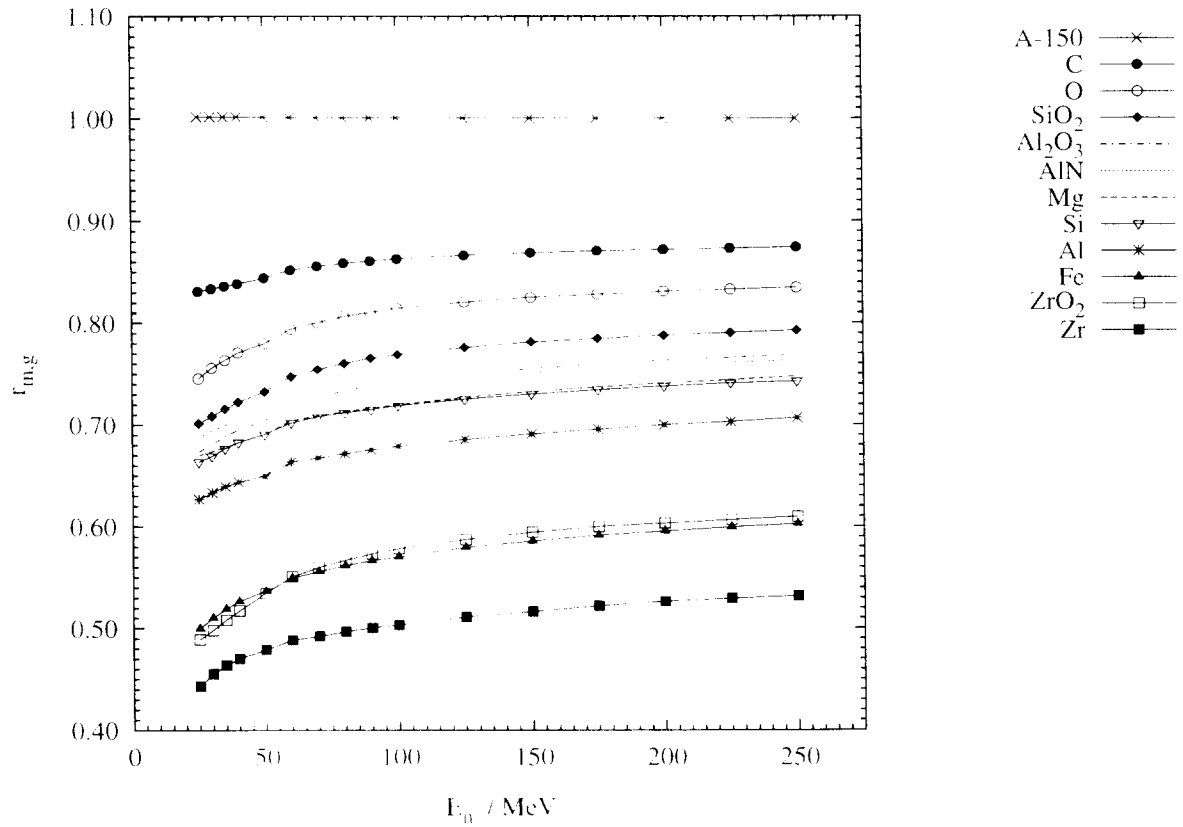
Figure 14: Calculated values of $r_{m,g}$ vs. neutron energy E_n for various wall materials m and methane-based tisue-equivalent gas g. The $r_{m,g}$ values were calculated with slowing-down spectral fluences based on LAHET calculations. mass stopping powers taken from TRIM [30]. and include treatment of HR ions.

Figure 15: Calculated values of $r_{m,g}$ vs. neutron energy E_n for various wall materials m and propane gas g. The $r_{m,g}$ values were calculated with slowing-down spectral fluences based on LAHET calculations. mass stopping powers taken from TRIM [30]. and include treatment of HR ions.

Figure 16: Calculated values of $r_{m,g}$ vs. neutron energy E_n for various wall materials m and propane-based tisue-equivalent gas g. The $r_{m,g}$ values were calculated with slowing-down spectral fluences based on LAHET calculations, mass stopping powers taken from TRIM [30], and include treatment of HR ions.
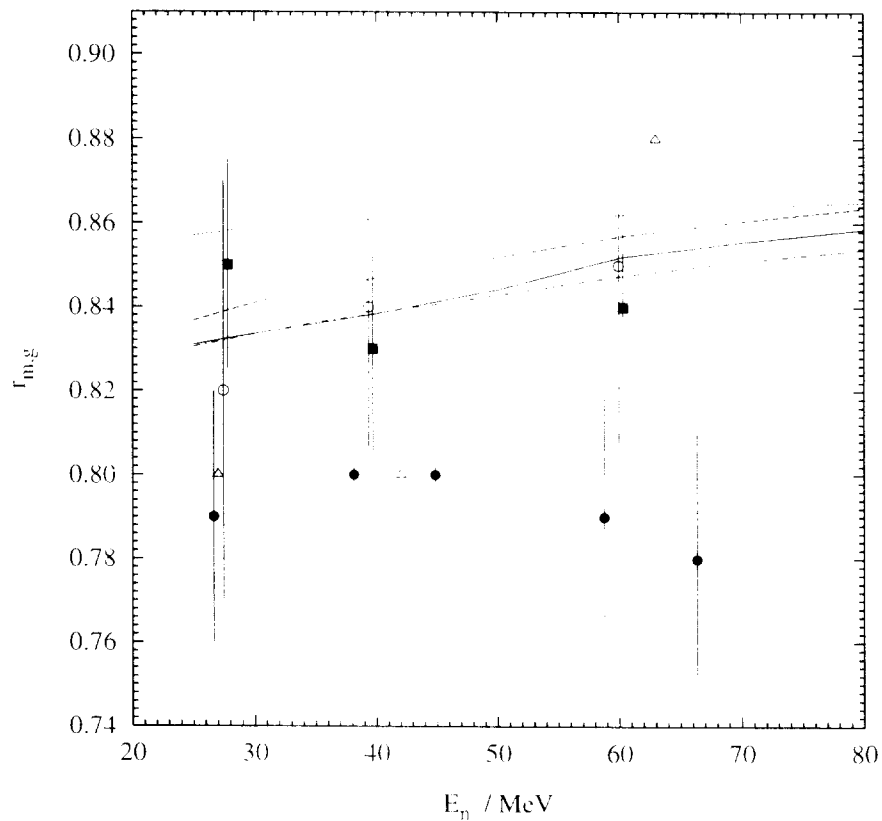
Figure 17: Present calculations of $r_{m,g}$ for C detectors with propane-based tissue-equivalent gas cavities including values based on data from LAHET [20] and TRIM [30] with HRs (—————). Values of $r_{m,g}^{l}$ are shown for calculations based on LAHET and TRIM data (— — — —). LAHET and ICRU [31] (—·—·—··), and based on data from ALICE [22] and Ref. [36] (···). Also shown are $r_{m,g}$ values from Menzel et al. (■) [13], Pihet and Menzel (○) [14], Pihet et al. (●) [15] and Binns and Hough (△) [18].

PTB-Berichte der Serie N (Neutronenphysik)

N-2: B. W. Bauer, W. G. Alberts, M. Luszig Bhadra,
B. R. L. Siebert:
**Experimental Investigation into the Influence of Neutron
Energy, Angle of Incidence and Phantom Shape on the
Response of Individual Neutron Dosemeters: Detailed
Analysis of Results for the Albedo Neutron Dosemeter in Use
at the PTB.**
54 S., 21 Abb., ISBN 3-89429-005-6, 1990, DM 20,50

N-3: H. Schumny:
**Personal Computers for Data Acquisition and Measurement,
Standards interfaces, State of the Art, Trends, Applications.**
66 S., 24 Abb., 5 Tab., ISBN 3-89429-009-9, 1990, DM 23,50

N-4: D. R. Schlegel-Bickmann, H. J. Brede, S. Guldbakke, u. a.:
**Measurement of k_U-Values of Argon-Filled Magnesium
Ionisation Chambers.**
76 S., zahlr. Tab., ISBN 3-89429-063-3, 1990, DM 65,00

N-5: B. W. Bauer, B. R. L. Siebert, W. G. Alberts, u. a.:
**Experimental Investigation into the Influence of Neutron
Energy, Angle of Incidence and Phantom Shape on the
Response of Individual Neutron Dosemeters: Experimental
Procedure and Summary of Results.**
36 S., 5 Abb., 10 Tab., ISBN 3-89429-072-2, 1990, DM 17,00

N-6: B. R. L. Siebert, W. G. Alberts, B. W. Bauer:
**Computational Study of Phantoms for Individual Neutron
Dosimetry.**
40 S., 20 Abb., 10 Tab., ISBN 3-89429-073-0, 1990, DM 17,50

N-7: D. Schmidt, R. Böttger, H. Klein, R. Nolte:
**Investigation of the ^{9}Be(α, n) ^{12}C Reaction
I: Experimental Procedure and Uncertainties**
42 S., 22 Abb., ISBN 3-89429-176-1, 1992, DM 23,00

N-8: D. Schmidt, R. Böttger, H. Klein, R. Nolte:
**Investigation of the ^{9}Be(α, n) ^{12}C Reaction
II. Differential Cross Sections for $E_\alpha = 7.02 - 15.70$ MeV and
$E_{ex}(^{12}C) = 0.0, 4.439, 7.654, 9.641, 10.84, 11.83$ and
12.71 MeV.**
96 S., 44 Abb., 3 Tab., ISBN 3-89429-177-X, 1992, DM 32,00

N-9: R. Nolte, H. Schuhmacher, H. J. Brede, U. J. Schrewe:
**Neutron Spectrometry with Liquid Scintillation Detectors at
Neutron Energies between 20 MeV and 70 MeV
A Status Report.**
58 S., 17 Abb., ISBN 3-89429-328-4, 1993, DM 22,50

N-10: W. G. Alberts (Hrsg.):
**Investigation of Individual Neutron Monitors on the Basis of
Etched-track Detectors: The 1990 EURADOS-CENDOS
Exercise.**
136 S., ISBN 3-89429-198-2, 1992, DM 36,00

N-11: K. Weise, W. Wöger:
Eine Bayessche Theorie der Meßunsicherheit
34 S., ISBN 3-89429-227-X, 1992, DM 18,50

N-12: R. A. Hollnagel:
**Comparison of the Effective Dose, E, and the Effective Dose
Equivalent, H_E, from Neutron Irradiation with Special
Regard to the Dose from Induced Photons.**
54 S., 15 Abb., ISBN 3-89429-261-X, 1992, DM 22,50

N-13: H. Schuhmacher, U. J. Schrewe:
Dose Equivalent Measurements on Board Civil Aircraft.
42 S., 14 Abb., 5 Tab., ISBN 3-89429-306-3, 1993, DM 20,00

N-14: D. Schmidt, B. R. L. Siebert:
**Monte Carlo Simulation of Fast Neutron Scattering Experi-
ments Including DD-Breakup Neutrons.**
48 S., 34 Abb., ISBN 3-89429-332-2, 1993, DM 22,50

N-15: W. G. Alberts, H. Kluge:
**PTB-Vergleichsmessungen an Personendosimetern für
Neutronenstrahlung.**
40 S., 28 Abb., 12 Tab., ISBN 3-89429-352-7, 1993, DM 20,50

N-16: M. Weyrauch, K. Weise:
**Untersuchung der Unsicherheiten bei der Messung mit
Thermolumineszenz-Dosimetern.**
28 S., 3 Abb., ISBN 3-89429-374-8, 1993, DM 18,00

N-17: P. Mikula, V. Wagner, R. Scherm:
**On the focusing in neutron diffraction by elastically bent
perfect crystals.**
34 S., 15 Abb., ISBN 3-89429-478-7, 1994, DM 19,50

N-18: D. Schmidt, Xia Haihong:
Neutron Production by Deuteron Breakup on ^{4}He.
40 S., 15 Abb., ISBN 3-89429-536-8, 1994, DM 20,50

N-19: M. Matzke
**Unfolding of Pulse Height Spectra: The HEPRO Program
System.**
74 S., 7 Abb., ISBN 3-89429-543-0, 1994, DM 28,00

N-20: D. Schmidt, W. Mannhart, H. Klein, R. Nolte:
**Neutron Scattering on Natural Iron at Incident Energies
between 9.4 and 15.2 MeV.**
158 S., 59 Abb., ISBN 3-89429-552-X, 1994, DM 39,50

N-21: B. Wiegel, A. V. Alevra, B. R. L. Siebert:
**Calculations of the Response Functions of Bonner Spheres
with a Spherical ^{3}He Proportional Counter Using a Realistic
Detector Model.**
42 S., 29 Abb., 21 Tab., ISBN 3-89429-563-5, 1994, DM 31,50

N-22: A. V. Alevra, H. Klein, U. Schrewe:
**Measurements with the PTB Bonner Sphere Spectrometer in
High-Energy Neutron Calibration Fields at CERN.**
52 S., Abb., Tab., ISBN 3-89429-573-2, 1994, DM 23,00

N-23: M. Ginicke:
**Experimente zum Re-entrant - Spinglas Übergang am
System $(Fe_{65}Ni_{35})_{100-c}$ Mn_c – SQUID-Magnetometrie,
Mößbauereffekt, Neutronenspindepolarisation.** Dissertation.
180 S., 85 Abb., ISBN 3-89429-637-2, 1995, DM 41,50

N-24: K. Weise:
**Mathematical Foundation of an Analytical Approach to
Bayesian-Statistical Monte Carlo Spectrum Unfolding.**
52 S., ISBN 3-89429-967-3, 1995, DM 23,00

N-25: W. D. Newhauser, U. J. Schrewe, B. Wiegel:
**Gas-to-wall Absorbed Dose Conversion Factors for
Neutron Energies of 25 to 250 MeV.**
ca. 40 S., ISBN 3-89429-948-7, 1995, ca. DM 20,00